A&A 489, 571–581 (2008)
DOI: 10.1051/0004-6361:200810440

Astronomy & Astrophysics

The environmental dependence of properties of galaxies around the RDCSJ0910+54 cluster at $z = 1.1$⋆

M. Tanaka[1], A. Finoguenov[2,3], T. Kodama[4], T. Morokuma[4], P. Rosati[1], S. A. Stanford[5,6], P. Eisenhardt[7], B. Holden[8], and S. Mei[9,10]

[1] European Southern Observatory, Karl-Schwarzschild-Str. 2, 85748 Garching bei München, Germany
e-mail: mtanaka@eso.org
[2] Max-Planck-Institut für extraterrestrische Physik, Giessenbachstrasse, 85748 Garching bei München, Germany
[3] University of Maryland, Baltimore County, 1000 Hilltop Circle, Baltimore, MD 21250, USA
[4] National Astronomical Observatory of Japan, Mitaka, Tokyo 181-8588, Japan
[5] Institute of Geophysics and Planetary Physics, Lawrence Livermore National Laboratory L-413, 7000 East Avenue, Livermore, CA 94550, USA
[6] Department of Physics, University of California at Davis, 1 Shields Avenue, Davis, CA 95616, USA
[7] Jet Propulsion Laboratory, California Institute of Technology, Pasadena, CA 91109, USA
[8] UCO/Lick Observatories, University of California, Santa Cruz, CA 95065, USA
[9] University of Paris Denis Diderot, 75205 Paris Cedex 13, France
[10] GEPI, Observatoire de Paris, Section de Meudon, 5 place J. Janssen, 92195 Meudon Cedex, France

Received 23 June 2008 / Accepted 8 August 2008

ABSTRACT

We report on the environmental dependence of properties of galaxies around the RDCSJ0910+54 cluster at $z = 1.1$. We obtained multi-band wide-field images of the cluster with Suprime-Cam and MOIRCS on Subaru and WFCAM on UKIRT. Also, an intensive spectroscopic campaign was carried out using LRIS on Keck and FOCAS on Subaru. We collected 161 spectra with secure redshifts, with which we calibrated a larger sample of photometric redshifts. We discover a possible large-scale structure around the cluster in the form of three clumps of galaxies. Two out of the three newly discovered clumps of galaxies are detected as extended X-ray sources, suggesting that they are bound systems. There seem to be filaments of galaxies in between the clumps. This is potentially one of the largest structures found so far in the $z > 1$ Universe. We then examined stellar populations of galaxies in the structure. First, we quantified the color-radius relation. Red galaxies have already become the dominant population in the cores of rich clusters at $z \sim 1$, and the fraction of red galaxies has not strongly changed since then. The red fraction depends on the richness of clusters in the sense that it is higher in rich clusters than in poor groups. We confirm that this trend is not due to possible biases in photometric redshifts. Next, we examined red sequence galaxies. The luminosity function of red galaxies in rich clusters is consistent with one in local clusters. On the other hand, the luminosity function of red galaxies in poor groups shows a deficit of faint red galaxies. This confirms our earlier findings that galaxies follow an environment-dependent down-sizing evolution. Interestingly, the truncation magnitude of the red sequence appears brighter than found in the RDCS J1252−29 field at $z = 1.24$. This suggests that there is a large variation in the evolutionary phases of galaxies in groups with similar masses. Further studies of high redshift clusters will be a promising way of addressing the role of nature and nurture effects in shaping the environmental dependence of galaxy properties observed in the local Universe.

Key words. galaxies: evolution – galaxies: clusters: individual: RDCSJ0910+54 – cosmology: large-scale structure of Universe

1. Introduction

While galaxy clusters at $z > 1$ are now within our reach, larger scale structures are still difficult to locate and characterize. There are a handful of $z > 1$ clusters known to date and detailed analyses of their cluster galaxies have been made (e.g., Blakeslee et al. 2003; Lidman et al. 2004; Rosati et al. 2004; Nakata et al. 2005; Stanford et al. 2005, 2006; Mei et al. 2006a,b; Demarco et al. 2007; Tanaka et al. 2007b; Andreon et al. 2008). There is clear evidence that red early-type galaxies have become a dominant population by $z = 1$ in rich clusters. A tight red sequence has already been in place (e.g., Blakeslee et al. 2003; Lidman et al. 2004) and spectra of $z \sim 1$ cluster galaxies do not typically show signs of active star formation (Mullis et al. 2005; Demarco et al. 2007). The majority of cluster galaxies seem to have become red and dead by $z = 1$.

While rich clusters have been intensively studied, poor groups at $z > 1$ largely remain unexplored. This has been hampered by the fact that high redshift poor groups are difficult to find. But the recent advent of large telescopes with wide-field capabilities along with deep X-ray surveys have pushed studies of poor groups beyond a redshift of unity. These high-redshift, poor groups are particularly interesting since they should be the precursors of present-day clusters with moderate masses. Furthermore, there is some observational evidence that galaxy properties depend on cluster richness in the sense that cluster galaxies are more evolved than group galaxies (Zabludoff & Mulchaey 1998; Tran et al. 2001; Merchán & Zandivarez 2002; Balogh et al. 2002; Martínez et al. 2002; Tanaka et al. 2005, 2007b; Koyama et al. 2007; Gilbank et al. 2008). Galaxies in

⋆ Full Table 2 is only available in electronic form at http://www.aanda.org

rich clusters and in poor groups may follow different evolutionary paths. Therefore, it is essential to observe the full range of local galaxy density at various redshifts up to and beyond $z \sim 1$.

We are undertaking a high-redshift cluster survey with the Subaru telescope (Kodama et al. 2005), taking advantage of its wide-field imaging capabilities. Our aim is to observe a range of environments at various redshifts and improve our understanding of galaxy evolution as a function of environment. As part of this survey, we have observed several high redshift clusters (Kodama et al. 2005; Nakata et al. 2005; Umetsu et al. 2005; Tanaka et al. 2005, 2006, 2007b,a; Koyama et al. 2007). In this paper, we focus on one of the $z > 1$ clusters from our sample, RDCSJ0910+54, which was discovered in the ROSAT Deep Cluster Survey (Rosati et al. 1998). Stanford et al. (2002) carried out spectroscopic follow-up observations of this cluster, which was confirmed to lie at $z = 1.1$, and present the results of a Chandra observation, which measured a relatively high X-ray temperature. Mei et al. (2006a) present a detailed analysis of the red sequence galaxies using high resolution ACS images. Following these studies, we carried out deep and wide-field observations of this cluster and we present combined analyses of the photometric and spectroscopic properties of galaxies over a wider field around the central cluster at $z = 1.1$.

The layout of this paper is as follows. We summarize our observations in Sect. 2. Section 3 describes photometric catalogs and photometric redshifts. Then, we present large-scale structures around the RDCSJ0910 cluster in Sect. 4. We carry out detailed analyses of the photometric and spectroscopic properties of galaxies in the structures in Sects. 5 and 6. Section 7 discusses implications of our results for galaxy evolution, and the paper is summarized in Sect. 8.

Unless otherwise stated, we adopt $H_0 = 70$ km s^{-1} Mpc^{-1}, $\Omega_M = 0.3$, and $\Omega_\Lambda = 0.7$. Magnitudes are on the AB system. We use the following abbreviations: CMD for color-magnitude diagram, and LF for luminosity function.

2. Observations

2.1. Imaging observations

We made Suprime-Cam observations in R and z bands in May 2005. Following this initial run, we carried out $VRiz$ bands observations with Suprime-Cam in November 2006, K_s-band observation with MOIRCS in February 2006, and K-band observation with WFCAM in March 2007. Most of the observations were carried out under good conditions. We followed a standard data reduction scheme with custom designed pipelines (Yagi et al. 2002). The PSF sizes vary from band to band and we smoothed them to a common seeing as detailed below. The photometric zero-points were derived from standard star observations for the optical images and from the 2MASS catalog (Jarrett et al. 2000) for the nearIR images. The Galactic extinction was corrected using the extinction map provided by Schlegel et al. (1998). Figure 1 shows the sky area covered by our data and Table 1 summarizes the exposure times and limiting magnitudes.

2.2. Spectroscopic observations

Follow-up spectroscopic observations were carried out with LRIS on Keck and FOCAS on Subaru. The LRIS observations are summarized in Mei et al. (2006a). Objects targeted for the observations are K-band selected ($K < 20.0$ on the Vega system), with a supplimental i-band selection to fill the masks. We did not give priorities to galaxies on the red sequence.

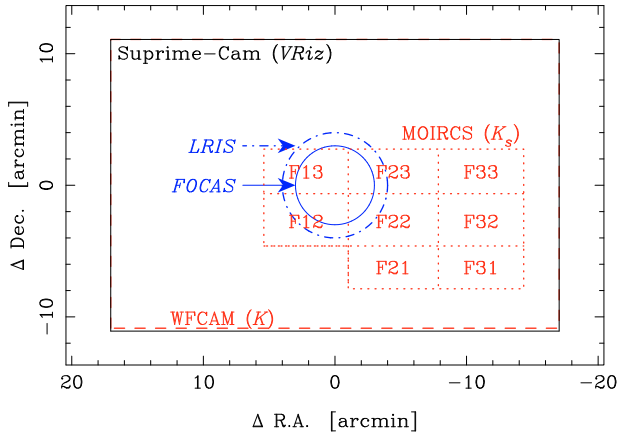

Fig. 1. The area of the sky covered by our data. The RDCSJ0910 cluster lies at (ΔRA, ΔDec) = (0′,0′). The solid, dashed, and dotted rectangles show the field coverages of Suprime-Cam ($VRiz$), WFCAM (K), and MOIRCS (K_s) images, respectively. We made an 8-pointing observation with MOIRCS as indicated by F12–F33. The solid circle shows the FOCAS field. We made several pointings with LRIS and the dot-dashed circle shows an approximate field coverage of the LRIS observations.

Table 1. Summary of the imaging data. The magnitude limits are 5σ limits in 2″ diameter apertures.

Observation	Exposure time	Magnitude limit
Suprime-Cam: V	60 min	26.6
Suprime-Cam: R	90 min	26.7
Suprime-Cam: i	45 min	26.2
Suprime-Cam: z	51 min	25.2
WFCAM: K	42 min	22.3
MOIRCS: K_s-F12	30 min	23.3
MOIRCS: K_s-F13	33 min	23.3
MOIRCS: K_s-F21	23 min	23.1
MOIRCS: K_s-F22	33 min	23.3
MOIRCS: K_s-F23	15 min	22.9
MOIRCS: K_s-F31	30 min	23.3
MOIRCS: K_s-F32	33 min	23.3
MOIRCS: K_s-F33	33 min	23.3

The FOCAS observations were made in April 2006 and December 2006 in MOS mode. We used the 300R grism with the SO58 order-cut filter. The slit width was set to 0.8″, which gave a resolution of $R \sim 500$. In the slit assignment, we gave the highest priority to bright ($z < 22.5$) galaxies on the red sequence in the $R-z$ color. The second priority was given to fainter ($22.5 < z < 23.5$) red sequence galaxies. We manufactured two masks both centered at the RDCSJ0910 cluster. One mask was exposed for 140 min and the other for 160 min. Observing conditions were good and the seeing varied between 0.7 and 1″.

The data reduction was performed in a standard manner. Fluxes were calibrated with standard stars observed each night. Telluric extinctions were not corrected. The Galactic extinction was corrected assuming the extinction curve derived by Cardelli et al. (1989). We visually inspected all the spectra and assigned redshifts and confidence flags with custom designed software.

We obtained 161 secure redshifts out of 237 galaxies observed in total. We estimated possible redshifts for 22 galaxies, and the rest of the galaxies have no secure/possible redshifts. As we discuss later, we use photometric redshifts to extract galaxies around the cluster redshift. 32 galaxies at $0.92 \leq z_{\rm phot} \leq 1.12$ were observed, out of which we obtained 22 secure, 4 possible, and 6 no redshifts. Only one of the 22 secure redshifts lies

Table 2. Spectroscopic catalog. The columns show object ID, coordinates in J2000, redshift, confidence flag (0 and 1 mean secure and possible redshifts, respectively), and aperture magnitudes within 2″ apertures and their errors. The systematic zero point errors are not included here. The redshift error does not include wavelength calibration error, which is typically 0.3 Å. Full Table 2 is available in electronic form.

ID	RA	Dec	redshift	flag	V	$\sigma(V)$	R	$\sigma(R)$	i	$\sigma(i)$	z	$\sigma(z)$	K	$\sigma(K)$
LRIS-8	09 10 47.5	54 17 04	$0.6122^{+0.0002}_{-0.0002}$	1	23.65	0.02	22.83	0.01	22.43	0.01	22.19	0.01	21.14	0.08
LRIS-9	09 10 51.7	54 22 18	$0.0000^{+0.0000}_{-0.0000}$	0	20.87	<0.01	20.02	<0.01	19.44	<0.01	19.11	<0.01	17.91	0.01
LRIS-11	09 10 38.2	54 22 39	$0.0000^{+0.0000}_{-0.0000}$	0	23.00	0.01	21.93	<0.01	20.27	<0.01	19.57	<0.01	18.55	0.01
LRIS-14	09 10 39.6	54 21 48	$0.0000^{+0.0000}_{-0.0000}$	0	21.74	<0.01	20.93	<0.01	20.08	<0.01	19.66	<0.01	19.03	0.02
LRIS-33	09 10 46.5	54 21 41	$1.1000^{+0.0001}_{-0.0001}$	0	24.66	0.04	23.70	0.01	22.94	0.01	22.04	0.01	20.68	0.06
LRIS-40	09 10 41.4	54 20 33	$0.6299^{+0.0002}_{-0.0002}$	0	23.27	0.01	22.45	0.01	22.02	0.01	21.78	0.01	20.84	0.06
LRIS-42	09 10 48.0	54 22 21	$0.0000^{+0.0000}_{-0.0000}$	0	22.73	0.01	22.53	0.01	22.33	0.01	21.83	0.01	20.44	0.05
LRIS-47	09 10 45.9	54 22 20	$1.1047^{+0.0006}_{-0.0024}$	0	26.04	0.13	24.18	0.02	23.65	0.02	22.50	0.02	20.69	0.06
LRIS-49	09 10 50.0	54 22 18	$0.2205^{+0.0001}_{-0.0002}$	0	22.23	<0.01	22.04	<0.01	21.94	<0.01	21.98	0.01	21.72	0.12
LRIS-60	09 10 41.1	54 22 19	$0.4352^{+0.0001}_{-0.0001}$	0	22.88	0.01	22.45	0.01	22.30	0.01	22.15	0.01	21.43	0.10

outside of the photo-z range. Three objects were observed with both LRIS and FOCAS, only one of which has secure redshifts: LRIS-1101 and FOCAS-2-11. Its redshifts from the LRIS and FOCAS observations are $1.0988^{+0.0003}_{-0.0003}$ and $1.0991^{+0.0022}_{-0.0018}$, being fully consistent within the error. We present in Table 2 the catalog of the spectroscopic objects. This includes 161 secure redshifts and 22 possible redshifts.

2.3. X-ray observations

The field was serendipitously covered by XMM-Newton observations of XY UMA on March 28 2005. The observational ID is 02009601. Medium filter was used for pn, MOS1 and MOS2 detectors with the corresponding net time after removal of flared time intervals of 48.5, 56.9 and 54.3 ksec. PN detector clocking mode was FullFrame. Using the approach developed in Finoguenov et al. (2007 and in prep.), we searched for the extended X-ray sources in the image. In detail, we removed read-out artifacts, detector background and sky background from each detector and perform a sophisticated point source flux removal from the scales of interest to extended source search using wavelets. We note that the XMM data cover a wider area than the Chandra data presented in Stanford et al. (2002). Sixteen extended sources are found, of which one is identified as the RDCSJ0910 cluster. Out of 4 galaxy clumps reported in this paper, X-ray emissions are detected from three of them and a filament between the two of them. Further discussions of these detections are presented in Sect. 4.

3. Catalog construction and photometric redshifts

3.1. Catalog construction

We have two K-band images, namely, from WFCAM and from MOIRCS. Since the field coverage, depth, and seeing sizes are different, we made two photometric catalogs; $VRizK$ (Suprime-Cam+WFCAM) and $VRizK_s$ (Suprime-Cam+MOIRCS). We refer to them as the WFCAM catalog and the MOIRCS catalog, respectively.

WFCAM catalog

The seeing size on the WFCAM image is 1.1″. We smoothed all the Suprime-Cam images to this seeing size (note that the original seeing of the optical images is 0.8″). We detected galaxies in the z-band since this is deeper than the WFCAM K-band image for red galaxies at $z = 1.1$. We then applied a magnitude cut of $z < 25.2$ (5σ) to the catalog.

MOIRCS catalog

The MOIRCS seeing varies from one field to another, and we smoothed the images to a common 0.8″ seeing size. The Suprime-Cam images were not smoothed because all of them have a seeing size of 0.8″. The MOIRCS images are deeper than the WFCAM image and we detected galaxies in the MOIRCS K_s-band. The exposure times of the K_s band vary from field to field (see Table 1). We further subdivided the catalog into two: MOIRCS-shallow ($K_s < 22.9$ for all the fields) and MOIRCS-deep ($K_s < 23.3$ and F21 and F23 are not used) to fully exploit the data.

In both catalogs, we used SExtractor for the object detection (Bertin & Arnouts 1996). We use MAG_AUTO for total magnitudes and 2″aperture magnitudes for colors. The photometric errors were derived from the standard deviation of sky fluxes in 2″apertures. The Poisson noise of each object's flux was then added in quadrature. Stars were removed on the basis of their compactness and colors.

As we will show later, we perform statistical subtraction of fore-/background galaxies. We use the data from the Subaru Deep Field (SDF) for this job. The data were kindly provided by the SDF team. We applied the same magnitude cuts to the SDF catalog as the WFCAM and MOIRCS catalogs to make fair samples of the control field.

3.2. Photometric redshifts

We apply the photometric redshift (photo-z) technique to largely eliminate fore-/background contamination. A custom designed photo-z code was developed for this purpose. The code follows the standard procedure. Each object is fitted with templates of galaxy spectral energy distributions and the redshift of the best-fitting template is used as photo-z.

A library of templates is made with Bruzual & Charlot (2003) models. We assume the τ model[1] to describe the star formation histories of galaxies. The parameter τ ranges from 0 (instantaneous burst) to ∞ (constant star formation rate). The dust extinction is taken into account except for $\tau = 0$ models assuming the Charlot & Fall (2000) extinction model. The optical depth in the V-band is allowed to vary between 0 and 5. We assume the Chabrier (2003) initial mass function and solar

[1] A star formation rate is proportional to $\exp(-t/\tau)$.

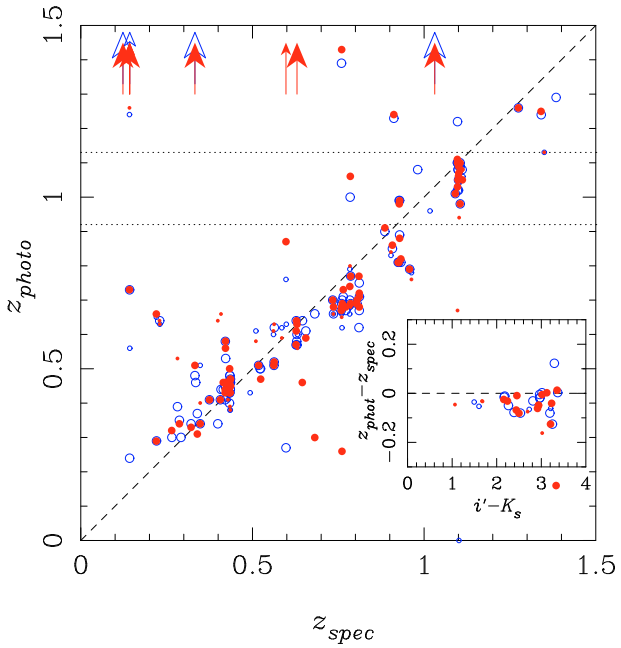

Fig. 2. Photometric redshift plotted against spectroscopic redshift. The open and filled points show photo-z based on WFCAM and MOIRCS-shallow catalogs, respectively. As discussed in Sect. 3.1, we made two different photometric catalogs for the two different sets of near-IR imaging data. The large/small symbols show galaxies brighter/fainter than $K = 21$. The open and filled arrows show data points that lie above the plotted range. The dashed line shows the $z_{\rm phot} = z_{\rm spec}$ relation. The horizontal dotted lines show our photo-z selection range to extract galaxies at $z = 1.1$. The inset shows the color dependence of our photo-z at $1.0 < z < 1.2$.

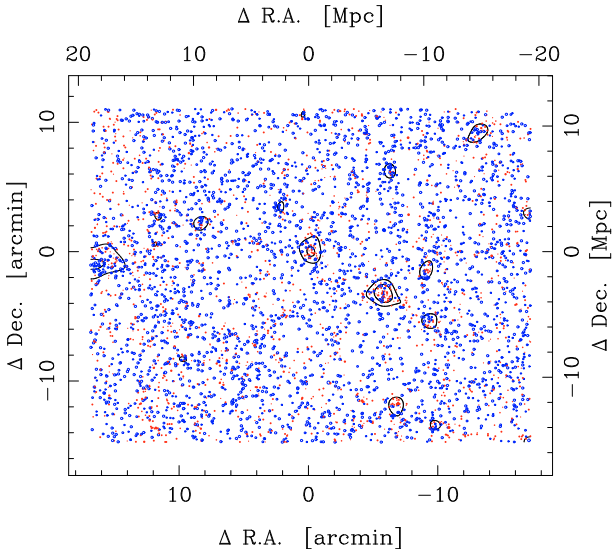

Fig. 3. Distribution of the photo-z selected galaxies in the RDCSJ0910 field ($0.92 \leq z_{\rm phot} \leq 1.12$). This is based on the WFCAM catalog. The galaxies are sorted into red and blue by their $R - z$ color and shown as filled and open points, respectively. The contours show galaxy densities at 2.5, 5, and 10σ levels estimated by smoothing the galaxy distribution with a 0.5 Mpc Gaussian kernel. The RDCSJ0910 cluster lies at (ΔRA, ΔDec) = (0′,0′). The top and right ticks show comoving scales.

and sub-solar metallicities ($Z = 0.02$ and 0.008) for the models. Although the intergalactic extinction is not particularly important for the purposes of the paper, we implement the extinction following Furusawa et al. (2000) with the extinction formula by Madau (1995). Each model is then convolved with the response functions of the filter, CCD and atmosphere (we assume airmass = 1) and a library of synthesized magnitudes is generated. Each observed object is then fitted with all the templates and the best-fitting model is searched for based on the χ^2 statistics.

We added 0.03 mag errors in quadrature to the photometric errors in all the bands to account for systematic zero point errors. There is often a mismatch between observations and model templates and we examined a possible mismatch in our data by offsetting observed data points and checking the resultant photo-z. We find that the magnitude shifts of $\Delta V = +0.1$ and $\Delta K = +0.3$ mag minimize the catastrophic failures. We applied these shifts for the photo-z purpose only (i.e., magnitudes in the following analyses are not shifted). These procedures were applied in both WFCAM and MOIRCS catalogs.

Figure 2 shows the accuracy of our photo-z estimates. Strongly blended objects are removed from the plot. The data points show a large scatter at $z < 0.5$. This is because we do not have the U and B bands, which are crucial for low-z objects. There is no contamination from $z < 0.5$ galaxies to $z \sim 1.1$. At $z > 0.5$, we tend to underestimate the true redshifts. But, this not an issue for our purpose of extracting galaxies at $z = 1.1$ either because the systematic offset in the photometric redshifts is known and we can adjust the photo-z selection range accordingly.

The chosen photo-z range to extract $z = 1.1$ galaxies is a trade off between completeness and contamination. A narrow range will give us a low contamination rate with low completeness, and a wide range will give us the opposite. In this paper, we prefer to be as complete as possible while maintaining the contamination minimal. We extract galaxies at $0.92 \leq z_{\rm phot} \leq 1.12$ as indicated by the horizontal dotted lines in Fig. 2. The fraction of $z = 1.1$ galaxies missed from this photo-z range is 11% and 5% for the WFCAM and MOIRCS catalogs, respectively. The fraction of contaminant galaxies (i.e., galaxies outside the $z = 1.1$ structure) within the photo-z range is 26% and 18%, respectively. We statistically subtract this remaining contamination as detailed below.

We note that the accuracy of photo-z is dependent on magnitudes and colors of galaxies. Photo-z becomes less accurate at fainter magnitudes due to increased photometric errors. Also, photo-z can be less accurate for blue galaxies (Tanaka et al. 2005, 2006). We quantified this magnitude and color dependence with the MOIRCS-shallow catalog (the WFCAM catalog follows a similar trend to the MOIRCS-shallow one). A fraction of $z = 1.1$ galaxies missed from the photo-z range is 0% and 17% for $K_s < 21$ and $K_s > 21$ galaxies, respectively. The fraction of contaminant galaxies is 19% and 17% for bright and faint galaxies, respectively. We do not observe strong color dependence as shown in the inset, although we have too few blue galaxies to fully address the color dependence. As shown later, the statistical field subtraction without using photo-z gives consistent results to those obtained using photo-z. Therefore, our results presented below are not strongly biased by photometric redshifts.

4. Large-scale structure at $z = 1.1$

We extract galaxies near the cluster redshift and present a potential large-scale structure around the RDCSJ0910 cluster in Fig. 3. The RDCSJ0910 cluster lies at (ΔRA, ΔDec) = (0′, 0′). We discover a cluster candidate at (ΔRA, ΔDec) = (−6′, −3′), and two more clumps can be seen at NW and SW of this cluster. These newly found systems show clear concentrations of red galaxies, which suggest that they are bound systems. These

clumps are closely clustered together, making it an interesting field at $z = 1.1$.

Figure 4 shows the same structure in the MOIRCS field. Refer to Fig. 1 for the overlap of the WFCAM and MOIRCS fields. Figure 5 presents a pseudo-color picture of the field. The MOIRCS images cover all the newly found systems. We dub the clumps number 1 to 4 as shown in the figure. Since the photo-z with the MOIRCS catalog is more accurate than the WFCAM catalog for faint galaxies (faint galaxies are not detected in the WFCAM image and hence do not have K-band photometry) and galaxies are detected in the K_s band (which suppresses foreground contamination), the structure is more clearly seen.

The photo-z selected galaxies seem to show filaments in between the clumps (see the 1σ density contours in Fig. 4). The filament around clump 1 extends in the N-S direction and it bends south towards clump 2. Possible filaments can be also seen between clump 2, 3, and 4. There seems to be a clump to the southeast of clump 1. However, this is not seen in the WFCAM map or X-ray map (Figs. 3 and 4) and it is close to the field edge. We do not discuss this clump further in the following.

An effective way to see if the systems are physically bound or not is to look for extended X-ray emissions. We show in Fig. 4 X-ray emissions as shades. The X-ray properties of the clumps are summarized in Table 3. The RDCSJ0910 cluster is clearly detected in X-ray. The newly found clump 2 also shows an extended emission and has a similar mass to the RDCSJ0910 cluster mass, $M_{500} \sim 9{\times}10^{13}\ M_\odot$, assuming that it lies at $z = 1.1$. clump 4 is also detected and has a smaller mass of $M_{500} \sim 5 \times 10^{13}\ M_\odot$. The remaining one, clump 3, is not detected at a 3σ level. Therefore, at least two of the three new systems are physically bound.

We are not yet sure if the newly discovered clumps lie at the same redshift and form a single structure due to the limited accuracy of photometric redshifts. We have carried out spectroscopic campaigns of this field, but so far we have focused on the main RDCSJ0910 cluster (clump 1) and we have not yet obtained spectra of galaxies in the newly found clumps. Although this is likely a real structure given that there seems to be filaments in between the clumps, we defer a firm conclusion on this point to future spectroscopic observations.

In the rest of the section, we discuss spectroscopically confirmed members in the main RDCSJ0910 cluster. Figure 6 shows the distribution of spectroscopic galaxies. We carried out intensive spectroscopic follow-up observations around the RDCSJ0910 cluster. The LRIS observations are described in Mei et al. (2006a). We obtained 20 cluster members, out of which 10 lie within r_{200} from X-ray. The members are indicated by the stars in the plot. The N-S extension around the cluster is also seen in the distribution of spectroscopically confirmed members. It is interesting to note that the filament towards the SW is also seen in the X-ray data (Fig. 4).

Using galaxies at $1.07 < z_{\rm spec} < 1.13$, the redshift and velocity dispersion of the RDCSJ0910 cluster is $z = 1.1005 \pm 0.0016$ and 716 ± 141 km s^{-1}, respectively. We used the biweight estimator for these estimates and the errors are jackknife errors (Beers et al. 1990). We also quote some relevant numbers here: $r_{200} = 0.95 \pm 0.19$ Mpc, and $M_{200} = 3.4^{+2.4}_{-2.1} \times 10^{14}\ M_\odot$ (Carlberg et al. 1997). These numbers appear larger than those estimated with X-ray ($r_{200} = 0.59$ Mpc and $M_{200} = 1.2 \times 10^{14}\ M_\odot$), suggesting that the cluster may have substructure and/or dynamically young.

To sum up this section, we discovered the potential clumpy and filamentary structure around the RDCSJ0910 cluster based on the wide-field multi-band data. If confirmed to be real, this will be among the few supercluster scale structures found so far in the $z > 1$ Universe.

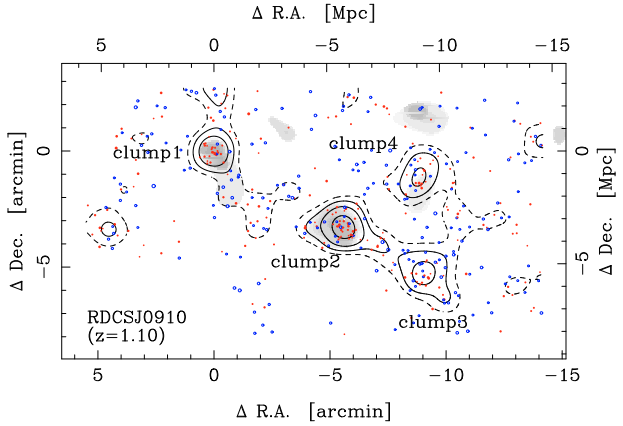

Fig. 4. Same as Fig. 3, but with the MOIRCS-shallow catalog. The galaxies are sorted into blue and red by their $i - K_s$ color following the definition of red galaxies in Sect. 5 and are plotted as the filled and open points. The dashed contours show 1σ over-density regions. The shades show X-ray emissions detected by XMM.

5. Environmental dependence of galaxy colors at $z = 1.1$

We examine the environmental dependence of galaxy colors at $z \sim 1.1$ in this section. First, we study the 'traditional' color-radius relation. We covered the surrounding regions of the newly found clumps, and we take this opportunity to examine colors of galaxies out to large radii at this high redshift. We then focus on color-magnitude diagrams (CMDs) of galaxies in the clumps.

5.1. Color-radius relation

We extract $z \sim 1.1$ galaxies with photo-z in the MOIRCS-shallow catalog. Since the masses of the newly found clumps differ from one another, we take r_{200} estimated using X-ray to normalize the cluster-centric radius. The clump 3 is not detected in X-ray and we take the 3σ limit for this clump.

We plot in Fig. 7 the fraction of red galaxies as a function of distance from the clump centers in units of r_{200}. Red galaxies are defined as those with $\Delta|i - K_s| < 0.5$ from the red sequence (see below). In this plot, the statistical field subtraction is not performed[2]. The fraction stays constant at $r/r_{200} \gtrsim 1$ and it increases at smaller radii reaching to 80% in the cores. Galaxies in the cores of clusters at $z \sim 1.1$ are almost exclusively red. The fraction sharply changes at $\sim r_{200}$ and it converges to the field value at this radius. The fraction at large radii is slightly higher than the control field value. This may suggest that galaxies in the filaments have a higher red fraction.

We also plot galaxies from the Sloan Digital Sky Survey for a $z = 0$ counterpart (York et al. 2000). The data were taken from the sixth data release (Adelman-McCarthy et al. 2007). We retrieved galaxies at $0.020 < z < 0.035$ from the Main Galaxy Sample (Strauss et al. 2002). To mimic the selection

[2] A significant fraction of galaxies at large radii is expected to be fore-/background galaxies, and the subtraction of them results in a large scatter with large errors in the data points. Thus, we do not subtract them and instead we draw the red fraction of the control field as the horizontal line.

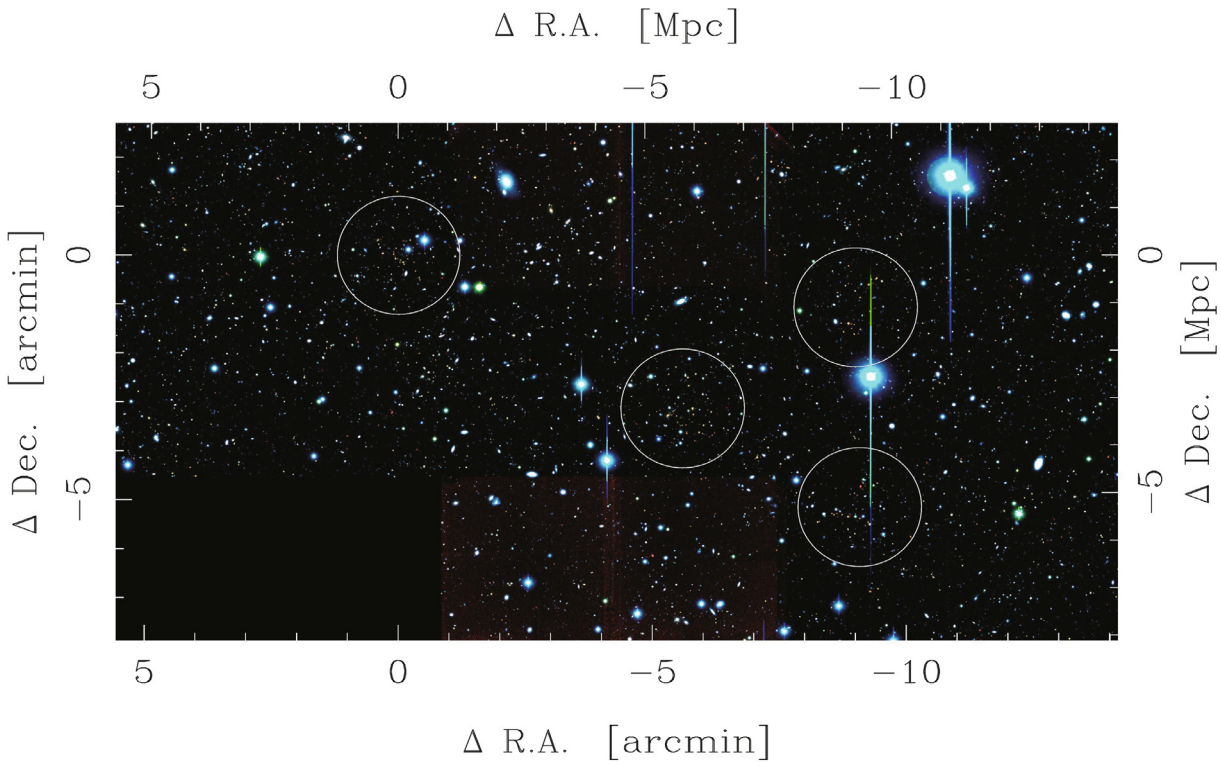

Fig. 5. RzK_s pseudo-color image of the RDCSJ0910 field. The circles show the four clumps. The top and right ticks show comoving scales.

Table 3. X-ray properties of the four clumps (see Fig. 4 for the definition of the clumps). Clump 3 is not detected in the X-ray data, and the numbers quoted below are 3σ limits. The coordinates correspond to the peak of the X-ray emission. The L_X luminosity is based on the extrapolation of the detected flux to R_{500}, described in Finoguenov et al. (2007). The total mass is computed using the scaling relations ($L_X - M$) with the weak lensing calibration for mass from COSMOS, achieved at a similar redshift ($z \sim 0.9$) and luminosity range (Leauthaud et al. in prep.). The newly discovered clumps are assumed to lie at the same redshift as the RDCSJ0910 cluster (i.e., clump 1).

clump	RA	Dec	L_X (10^{43} ergs s^{-1})	M_{500} (10^{13} $M_\odot$)
1	$09^h\ 10^m\ 45^s$	54° 22′ 08″	7.3 ± 0.9	8.9 ± 1.0
2	$09^h\ 10^m\ 09^s$	54° 18′ 56″	7.5 ± 1.1	9.0 ± 1.1
3	$09^h\ 09^m\ 44^s$	54° 20′ 22″	$<3.4 \pm 1.1$	$<4.8 \pm 1.2$
4	$09^h\ 09^m\ 45^s$	54° 16′ 50″	3.8 ± 1.3	5.2 ± 1.4

bias in the galaxies in the RDCSJ0910 field, we derived magnitudes in the i and K_s bands redshifted to $z = 1.1$ using KCORRECT (v4_1_4; Blanton et al. 2003). We fitted the Schechter function to the redshifted K_s band luminosity function and derived $M^*_{K_s,z=1.1} = -21.96$. We then applied a magnitude cut of $M_{K_s,z=1.1} < M^*_{K_s,z=1.1} + 2.4$ to cover the same magnitude range as the $z = 1.1$ sample[3].

Galaxy groups were identified via the friends-of-friends algorithm (Ramella et al. 1997; Diaferio et al. 1999; Merchán & Zandivarez 2002). For the line-of-sight and transverse linking lengths, we adopted 500 km s^{-1} and 500 kpc, respectively. This technique was applied to the volume-limited sample and the linking lengths do not change with redshift. Systems with more than 5 members were identified. These are the same parameters we adopted in Tanaka et al. (2005). For each system, the velocity dispersion and r_{200} were estimated with the gapper method (Beers et al. 1990). Low mass systems ($\sigma < 500$ km s^{-1}, which roughly corresponds to $M_{200} < 10^{14}$ $M_\odot$) were removed for a fair comparison with the $z = 1.1$ systems.

In the local Universe, the fraction of red galaxies converges to the field value around $\sim 1.5 r_{200}$, being consistent with earlier studies (e.g., Carlberg et al. 1997; Tanaka et al. 2004; Rines et al. 2005). Compared to this local value, the $z = 1.1$ systems converge to the field value at smaller radii ($\sim r_{200}$). But, this may be due to contamination of fore-/background galaxies since the fraction of contaminant galaxies increases in the outskirts. The red fraction in the field is higher at $z = 0$ than at $z = 1.1$, reflecting the decrease in the cosmic star formation rate. In contrast to this, the red fraction in the cores does not strongly evolve since $z = 1.1$. The cluster cores at $z = 1.1$ are already dominated by red galaxies.

Let us be more quantitative about this trend. We find that the fraction of red galaxies corrected for the field contamination in the combined clumps 1–4 within r_{200} is 0.72 ± 0.03. The $z = 0$ rich systems have a similar fraction of 0.82 ± 0.05. The red fraction shows only a small change since $z = 1.1$. If we focus on rich systems (clumps 1 and 2), the red fraction is 0.80 ± 0.04, which is consistent with the local value. This suggests that red galaxies have already become a dominant population in rich clusters

[3] The K_s-band characteristic magnitude of $z \sim 1.1$ galaxies is $m^*_{K_s} = 20.5$ (Strazzullo et al. 2006) and we reach $m^*_{K_s} = 22.9$ ($= m^*_{K_s} + 2.4$) with the MOIRCS-shallow catalog. We applied the same magnitude cut relative to the characteristic magnitude to the sloan catalog.

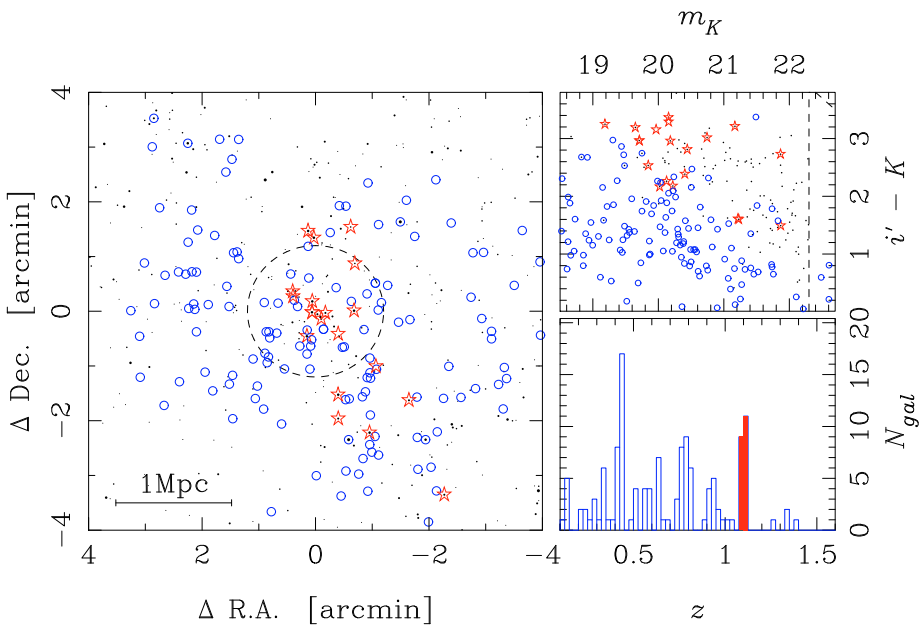

Fig. 6. Distribution of galaxies with spectroscopic and photometric redshifts around the RDCSJ0910 cluster. *Bottom-right:* redshift distribution of the spectroscopic galaxies. The filled histogram shows the $z = 1.1$ structure. Galaxies inside/outside the filled histogram are shown as stars/open circle in the other panels. *Top-right:* $i - K$ color plotted against K magnitude. The black dots are photo-z selected galaxies. The dashed lines show the 5σ magnitude and color. *Left:* spatial distribution of the spectroscopic galaxies. The dashed circle shows r_{200} of the cluster estimated from our X-ray data. The 1 Mpc physical scale is shown at the *bottom left*.

at $z = 1.1$ and no significant evolution is seen in the fraction of red galaxies. In other words, the environmental dependence of galaxy colors is already fully in place at $z = 1.1$. As discussed in Tanaka et al. (2006), the accuracy of photometric redshifts may depend on galaxy color so we may be missing some blue galaxies. Our current spectroscopic sample does not allow us to examine this point in detail because we have few spectroscopic galaxies at $z = 1.1$ with blue colors (see Fig. 6). But, we apply the statistical field subtraction without using photo-z and find a similar red fraction: 0.77 ± 0.08 for clump 1+2. Therefore, this high fraction is not due to possible photo-z biases, but is likely robust.

The poor systems (i.e., clumps 3 and 4) show a smaller red fraction of 0.59 ± 0.05 (the statistical subtraction gives 0.61 ± 0.10, again being consistent with that obtained with photo-z). The fraction of red galaxies is ∼35% higher in rich systems. Because we use the same data set for these two combined systems, the relative comparison between clumps 1 and 2 and clumps 3 and 4 is robust. A dependence of the stellar populations in the probable member galaxies on cluster richness also appears to be in place already at $z = 1.1$.

5.2. Color-magnitude diagrams

We now turn our attention to the color-magnitude diagrams of the galaxies. Since we have four galaxy systems at $z \sim 1.1$ with various masses, it is interesting to examine variations of galaxy colors and magnitudes in different systems. In this subsection, we use the MOIRCS-deep catalog. Note that this catalog covers all the clumps.

Figure 8 shows the CMDs of the clumps 1–4. We extract galaxies within r_{200} from the average center of the few brightest galaxies in each clump. r_{200} for each clump is estimated from the X-ray data. For clump 3, we use the 3σ upper limit on r_{200} since this is not detected at a significant level. r_{200} effectively covers the apparent extent of each clump as shown in Fig. 7. We make a combined clump of the clumps 1 and 2, both of which have similar masses (see Table 3). We do the same for clump 3 and 4.

A statistical field subtraction is performed in this plot following the procedure detailed in Tanaka et al. (2005). In short, the expected number of contaminant galaxies is estimated based on the average surface density of the control galaxies. The distribution of the control galaxies in the CMD is used as a probability map of contamination and the galaxies in the clumps are statistically subtracted according to their field probabilities. Figure 8 is one such realization of the statistical subtraction.

A clear sequence of red galaxies is observed in clumps 1 and 2. We apply the bi-weight fit to the sequence at $K_s < 22$ and obtain $i - K_s = -0.112^{+0.051}_{-0.049} \times (K_s - 20) + 2.86^{+0.06}_{-0.06}$. The errors are estimated by bootstrapping the input catalog. We take this as the best-fitting red sequence and plot it in Fig. 8. The slope is slightly steeper than our earlier measurement for the RDCSJ1252 cluster at $z = 1.24$ (slope of the $i - K_s$ color is $-0.058^{+0.026}_{-0.032}$; Tanaka et al. 2007b), but the slope observed here fits the RDCSJ1252 red sequence reasonably well. Galaxies at $K_s > 22$ in clumps 1 and 2 tend to be on the blue side of the sequence. One can fit a steeper slope using all the red galaxies down to the magnitude limit: slope $= -0.195^{+0.03}_{-0.03}$. But, this does not fit the RDCSJ1252 red sequence, suggesting that those faint red galaxies in the clump 1+2 may not have become fully red yet.

The red sequence in clumps 3 and 4 at $K_s < 22$ shows similar slope and offset to the clump 1+2 red sequence: $i - K_s = -0.099^{+0.072}_{-0.072} \times (K_s - 20) + 2.92^{+0.08}_{-0.08}$. The location of the red sequence on a CMD indicates the redshift of a system. Higher redshift clusters form an apparently redder sequence. The similarity of the locations of the sequences in these clumps suggests that they lie at similar redshifts.

To be quantitative about the red sequence, we measure the color scatter around the red sequence and show them in Table 4. The scatter is measured as follows. The input catalog is bootstrapped and the statistical field subtraction is performed. Then,

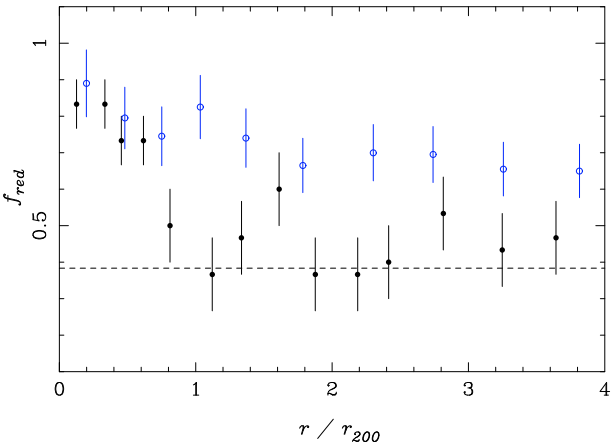

Fig. 7. Fraction of red galaxies plotted against cluster-centric radius. The filled points show galaxies at $z = 1.1$ and each bin contains 50 galaxies. The error bars show the Poisson errors. The horizontal dashed line shows the red fraction of the control field sample. Statistical field subtraction is not performed in this plot. The open points show $z = 0$ galaxies and each bin contains 200 galaxies.

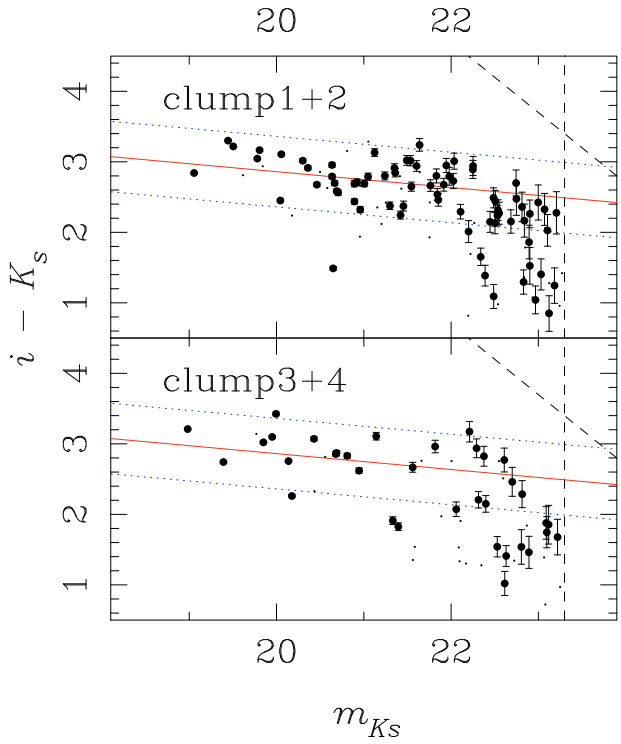

Fig. 8. $i-K_s$ color plotted against K_s magnitude. The dashed line shows the 5σ limiting magnitudes and colors. The solid line is the best-fitting red sequence in clump 1+2. The dotted lines show $\Delta(i-K_s) = \pm 0.5$ from the red sequence. The small dots are statistically subtracted galaxies.

the surviving galaxies within $|i - K_s| < 0.75$ of the red sequence are extracted. This color range is wide enough to include all red galaxies, while it is small enough to remove most of the blue galaxies. We apply 2σ clipping once to exclude outliers and measure the intrinsic scatter assuming $\sigma^2_{\rm measured} = \sigma^2_{\rm intrinsic} + \sigma^2_{\rm photometric\ error}$. This procedure is repeated 100 000 times and we take the median of the distribution of the color scatter as the estimate and a 68% interval as its error.

The scatter does not significantly increase down to the faintest magnitude bin in clumps 1 and 2, suggesting that the red sequence is already formed. Mei et al. (2006a) observe the tight red sequence in the $i-z$ color down to $z = 24$, which corresponds to $K_s \sim 22$ for red galaxies at $z = 1.1$, in the RDCSJ0910 cluster (i.e., clump 1). Our result appears consistent with their work, but we do not make any morphological selection, nor spectroscopic selection in this work. Dusty spirals and fore-/background contamination can increase the apparent color scatter here. Also, the $i-K_s$ color is more sensitive to age and dust effects than the $i-z$ color. Therefore, the comparison between their result and our result here is not straight forward. There is a hint of an increased scatter at $K_s > 21.3$ in the clump 3+4, although this is not statistically significant.

To further quantify the red sequence, we plot in Fig. 9 the luminosity function (LF) of red galaxies in the clumps 1+2 and 3+4. Here the red galaxies are defined as those within the $\Delta|i - K_s| < 0.5$ from the best-fitting red sequence (i.e., those between the dotted lines in Fig. 8). The LFs are normalized at $K_s = 20.0-20.5$ ($\sim M^*_{K_s}$, Strazzullo et al. 2006) for comparison. The LF of clump 1+2 is a smooth function with a hint of a slight decrease at the faint end ($K_s \gtrsim 22$). In contrast to this, the number of the red galaxies in the clump 3+4 starts to decrease at a brighter magnitude of $K_s \sim 21$ with some scatter at fainter magnitudes. This suggests that the red sequence is not fully in place at faint magnitudes in the clump 3+4.

We also plot red galaxies at $z = 0$ from the Sloan survey as the open squares in Fig. 9. We recall that we k-corrected the sloan photometry to probe the same rest-frame wavelength as the K_s-band for $z = 1.1$ galaxies. The magnitudes are plotted relative to the characteristic magnitudes at each redshift (the top ticks show apparent K_s band magnitudes of $z = 1.1$ galaxies). The LF of clump 1+2 is consistent with the sloan data, suggesting that the red sequence is fully built up by $z \sim 1$ in rich clusters at least down to $K^*_s + 2$ and massive cluster galaxies are already fully assembled. In contrast to this, the clump 3+4 shows a clear deficit of faint red galaxies. Faint galaxies are not yet assembled and/or are still blue in poor groups.

Another interesting way of quantifying the red sequence will be the ratio of luminous red galaxies to faint red galaxies. We define luminous and faint galaxies as $m_{K_s} < 21$ and $21 < m_{K_s} < 23.3$. The luminous to faint galaxies ratio is 0.48 ± 0.12, and 1.06 ± 0.47 for clump 1+2 and 3+4, respectively. Poorer systems tend to lack faint red galaxies.

As a sanity check, we derive LFs of red galaxies using the statistical field subtraction technique only. The LFs agree with those obtained with photo-z within the errors. The luminous to faint ratio is 0.51 ± 0.11 and 1.43 ± 0.46 for clump 1+2 and 3+4, respectively. The ratios are again in consistent within the error. We therefore suggest that our results are not strongly affected by biases in photometric redshifts.

The faint end of the red sequence is not fully in place in poor groups at high redshifts – this is consistent with our earlier work (Tanaka et al. 2005, 2007b). The red sequence in the clump 3+4 seems to be truncated at $K_s \sim 21$. Interestingly, this truncation magnitude is brighter than that we found in the RDCSJ1252 cluster at $z = 1.24$. In Tanaka et al. (2007b), we discovered four poor groups around the RDCSJ1252 cluster at $z = 1.24$. These groups have $M_{500} \sim 4 \times 10^{14}\ M_\odot$, which is similar to the clump4 mass. But, the red sequence in these groups is sharply truncated at $K_s = 22$, which is fainter by 1 mag. than that we found here. This suggests that there is a large variation in evolutionary phases of galaxies in $z \sim 1$ groups even if galaxies live in groups of similar masses. We defer discussions of implications of these results for galaxy evolution to Sect. 7.

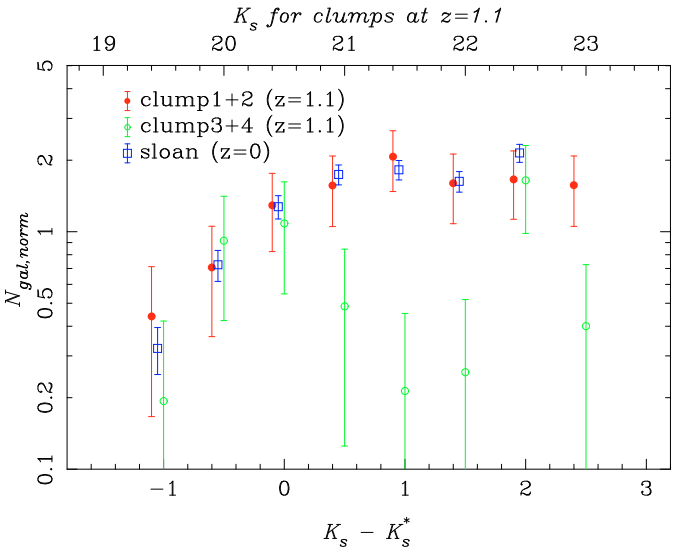

Fig. 9. LF of red galaxies. The filled points, open points, and open squares show the clump 1+2, clump 3+4, and the sloan data (i.e., $z = 0$) respectively. The magnitudes are plotted relative to the characteristic magnitudes at $z = 1.1$ for the clumps and $z = 0$ for the sloan data. We note that the sloan photometry is k-corrected to probe the same rest-frame wavelength as the K_s band for $z = 1.1$ galaxies. The LFs are normalized at $-0.5 < K_s - K_s^* < 0$. The top ticks show K_s magnitudes at $z = 1.1$. Note that the sloan data do not reach as deep as the MOIRCS-deep catalog. The points are slightly shifted horizontally in order to avoid overlapping. The error bars show the Poisson error.

Table 4. Intrinsic $i - K_s$ color scatter around the red sequence as a function of K_s band magnitude.

magnitude	clump 1+2	clump 3+4
19.3–20.3	$0.281^{+0.040}_{-0.021}$	$0.313^{+0.042}_{-0.025}$
20.3–21.3	$0.256^{+0.024}_{-0.025}$	$0.248^{+0.027}_{-0.052}$
21.3–22.3	$0.297^{+0.030}_{-0.034}$	$0.417^{+0.066}_{-0.079}$
22.3–23.3	$0.297^{+0.049}_{-0.055}$	$0.338^{+0.064}_{-0.079}$

6. Composite spectra of red galaxies

In this section, we study the spectroscopic properties of galaxies in the clumps. We present the composite spectrum of the RDCSJ0910 cluster (i.e., clump 1) red galaxies in Fig. 10. The red galaxies are defined as those within r_{200} (derived from the X-ray data) with colors of $|i - K_s| < 0.5$ from the red sequence. We excluded one AGN from the X-ray data presented in Stanford et al. (2002) and Mei et al. (2006a) from the following analysis. We smoothed the spectra to a common instrumental resolution of $R \sim 350$. Each spectrum was normalized to unity at 4000–4200 Å and 8 spectra were combined by taking a 2σ-clipped mean. For comparison, we also made the composite spectrum of red galaxies outside r_{200} using 5 galaxies. In what follows, we refer to the two composite spectra as cluster and field spectra for simplicity. It should be noted that some of the red galaxies outside r_{200} may be bound to the cluster and they may not be representative of the field galaxies.

Both spectra show a strong 4000 Å break with prominent CaIIHK lines, suggesting that galaxies are dominated by evolved stars. Their red colors are not due to strong dust extinctions. Although [OII] emissions are seen in a few individual spectrum, the composite spectra show no strong [OII] emissions and apparently red galaxies in and around clusters at $z = 1.1$ are not actively forming stars. Most at $z = 1.1$ have already suppressed their star formation.

This fact motivates us to fit a passive evolution model to the spectra and derive an average age of the red galaxies in two different environments. We use the Bruzual & Charlot (2003) model assuming passive evolution, solar metallicity, Chabrier IMF, and no dust extinction. The best-fitting model spectra is shown along with the observed composite spectra in Fig. 10. The model fits the overall continuum shape and some of the most prominent absorption lines such as G-band well. However, some differences between models and observations can be seen. For example, the CaIIHK absorptions are not fit very well by the models. Most of such differences will probably be due to strong sky lines in this wavelength region. We stack only 8 and 5 galaxies, and the effects of OH emissions cannot be completely removed.

The input spectra are bootstrapped and the models are fit for each composite spectrum. Then, the median and a 68% interval of the best-fitting age distribution are taken as an estimate and its error. The best-fitting age for the cluster red galaxies is $3.5^{+1.0}_{-0.5}$ Gyr, which suggests that the bulk of stars in the red galaxies formed at $z_f = 3.3^{+2.9}_{-0.6}$. This seems to be consistent with earlier studies of high redshift clusters (e.g., Blakeslee et al. 2003; Lidman et al. 2004; Holden et al. 2004; Mei et al. 2006a; Lidman et al. 2008; Mei 2008). In contrast to the cluster red galaxies, the field red galaxies show a younger age of $2.0^{+1.0}_{-1.0}$ Gyr, or $z_f = 1.9^{+0.8}_{-0.5}$. The field red galaxies are younger than the cluster red galaxies by 1.6 Gyr, although this is a statistically marginal difference. This age difference is roughly consistent with earlier studies (e.g., Thomas et al. 2005). We note that the age-sensitive Hδ absorption is stronger in the field red galaxies, which also suggests their younger age.

We note that the broad-band properties of these red galaxies in-/outside r_{200} are slightly different. The mean and dispersion of the K_s-band magnitudes and $i - K_s$ colors of these galaxies are $K_s = 20.4 \pm 0.7$ and $i - K_s = 2.94 \pm 0.25$ and $K_s = 19.9 \pm 0.5$ and $i - K_s = 3.07 \pm 0.29$ for cluster and field galaxies, respectively. The Mann-Whitney test shows that the probability that the magnitudes and colors are drawn from the same population is 10%. The colors of cluster and field red galaxies are consistent within the dispersion and the field red galaxies have slightly redder average color. Thus, the younger age of the field red galaxies is not due to color selection biases, but likely a real trend.

It would be interesting to see if there is any difference in stellar populations of galaxies in between poor groups and rich clusters. But, we do not yet have spectra of galaxies in the newly discovered clumps, and we defer discussions of spectral differences in different environments to a future paper.

7. Discussions

7.1. Comparisons with previous work

One of the primary findings of this work is that the environmental dependence of galaxy colors seems to be already in place in the $z = 1.1$ Universe. Rich clusters are already dominated by red galaxies and the fraction of red galaxies within r_{200} at $z = 1.1$ is similar to the fraction at $z = 0$, while the red fraction in the field significantly increases down to $z = 0$.

Our results might appear inconsistent with earlier work. For example, Cucciati et al. (2006) report that the color-density relation weakens at higher redshift. However, they examined the

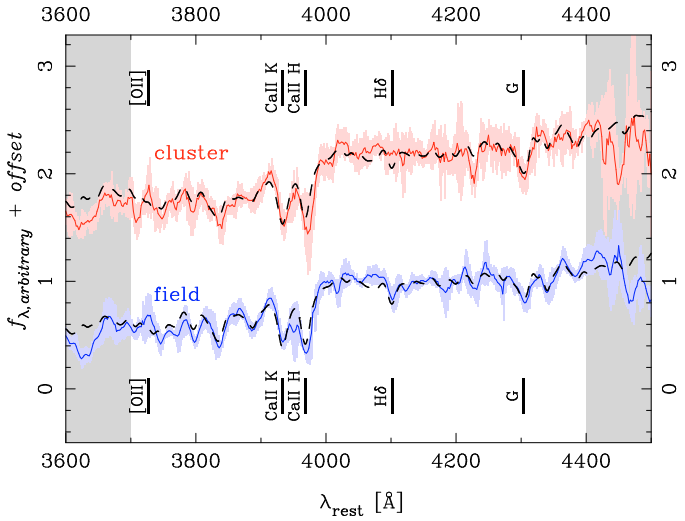

Fig. 10. Composite spectra of red galaxies within r_{200} from the clump 1 center (cluster) and outside r_{200} (field). The shades associated with the spectra show 1σ errors. The dashed lines show the best-fitting passive evolution model. The shaded regions on the right and left of the plot are not used in the fit since these regions are strongly affected by telluric absorptions and it is hard to calibrate fluxes well at long wavelengths ($\lambda_{obs} > 9000$ Å).

dependence of colors on large-scale environments (e.g., they defined environments with a 5 Mpc Gaussian aperture), and as remarked by them, their results cannot be extrapolated down to cluster scales.

Cooper et al. (2007) also show that the color-density relation weakens at higher redshifts based on the DEEP2 data (see also Gerke et al. 2007 for a similar result). There are two fundamental differences between our sample and theirs. Firstly, their galaxies are selected in the rest-frame B-band, while we use the K_s band, which corresponds to rest-frame 1 μm. The rest-frame B band detection can be affected by on-going star formation activity. They tend to trace blue galaxies and their density estimates are biased by the density of blue galaxies. The K_s-band selection will probably give a higher red fraction in high density regions. Secondly, they did not probe rich clusters, while we do. The range of environments explored in this paper is different from that explored by DEEP2. Therefore, we cannot make a fair comparison due to these differences and their results are not in apparent conflict with ours.

Elbaz et al. (2007) show that there is a moderate color-density relation at $z \sim 1$, but their red fraction in the highest density retion is not as high as we found in this paper. This is because they did not probe rich clusters. Recently, Cowie & Barger (2008) find no strong dependence of the red fraction on environment based on a K-band selected catalog. But, they did not probe rich clusters either.

7.2. Implications for galaxy evolution

We discovered three new clumps of galaxies near the RDCSJ0910 cluster. One of which has a similar mass to the RDCSJ0910 cluster mass, while the remaining two are lower mass systems. The rich systems at $z = 1.1$ seem to be fully evolved systems. They are dominated by red galaxies and the LF of red galaxies is nearly flat at faint magnitudes and is actually consistent with the local LF from the Sloan survey. This is also consistent with earlier findings that stellar mass functions of galaxies in rich clusters do not strongly evolve since $z \sim 1$ (e.g., Strazzullo et al. 2006). On the other hand, the poor groups at $z = 1.1$ exhibit a deficit of faint red galaxies. The red sequence is not yet fully in place at faint magnitudes in these systems. Also, the fraction of red galaxies is lower than clusters. It seems galaxies in lower density regions evolve more strongly at $z < 1$.

We suggested in our earlier papers that galaxy-galaxy interactions in low density environments such as groups and field may be the primary physical driver of the environmental dependence (Tanaka et al. 2006, 2007a). Our results in this paper seem to support this idea. The fraction of red galaxies increases in poor groups at lower redshifts, while that in rich clusters does not significantly increase. It is the group environment where environmental effects act on galaxies. Progenitors of rich clusters at $z = 1.1$ should be poor groups at higher redshifts and the cluster galaxies have already changed their properties by the time we observe them at $z = 1.1$. The most likely physical process will be galaxy-galaxy interactions because they should happen most frequently in groups and cluster-specific mechanisms such as ram-pressure stripping are unlikely to play a major role there. Galaxy-galaxy interactions may trigger intense starbursts, which may consume gas in galaxies. The subsequent star formation activities are suppressed due to lack of gas in galaxies. However, it will be essential to perform detailed spectral analyses of the galaxies in the poor groups at $z = 1.1$ to prove the scenario.

We now turn our attention to another interesting finding of this work. The rich systems exhibit the red sequence down to faint magnitudes, while the poor systems lack faint red galaxies. This is fully consistent with the picture of the build-up of the red sequence drawn in our earlier papers and those by other authors (Tanaka et al. 2005, 2007b; Koyama et al. 2007; Gilbank et al. 2008, but see also De Lucia et al. 2007). The red sequence is first built-up at bright magnitudes and extends to fainter magnitudes, and this build-up is "delayed" in poor systems.

But, there seems to be a large variation in evolutionary phases of galaxies at this redshift. We observed that the red sequence in poor systems around RDCSJ0910 is truncated around $K_s = 21$. In Tanaka et al. (2007b), we reported that the red sequence is sharply truncated at $K_s = 22$ in poor systems around the RDCSJ1252 cluster at $z = 1.24$. Although these systems have similar masses, the truncation magnitude appears to differ by $\Delta K_s \sim 1$. It seems that galaxies in the RDCSJ1252 groups are more evolved than those in the RDCSJ0910 groups, although the RDCSJ1252 lies at higher redshift (the time difference between $z = 1.24$ and $z = 1.1$ is ~0.5 Gyr).

We speculate that initial conditions of galaxy formation come into play here. The evolution of galaxies is determined by both nature and nurture effects. Our finding that galaxy properties can be quite different at high redshifts even if galaxies live in groups of similar masses seems to suggest that the nature effect plays a role in the $z > 1$ Universe. The structure around the RDCSJ1252 cluster at $z = 1.24$ is somewhat loose (Tanaka et al. 2007b). On the other hand, the structure around the RDCSJ0910 cluster reported in this paper is more compact and prominent. However, galaxies seem to be less evolved in the groups around the RDCSJ0910 cluster. This is somewhat contrary to what one may expect, but this probably means that we simply need much better statistics. There are a good number of $z > 1$ cluster candidates in large surveys such as COSMOS, and statistics will be improved in the near future. Further work on $z > 1$ clusters will be a promising way of addressing the origin of the environmental dependence of galaxy properties.

8. Conclusions

We carried out the intensive multi-band wide-field observations of the cluster RDCSJ0910 at $z = 1.1$ with Suprime-Cam, WFCAM, MOIRCS, FOCAS, and LRIS. The potential large-scale structure was discovered based on the photometric redshifts. Two of the three newly discovered systems show the extended X-ray emissions, suggesting that these are physically bound systems. There seems to be filaments in between the clumps. If confirmed to be real, this will be one of the most prominent structure ever found in the $z > 1$ Universe.

We then looked into properties of galaxies in the structure. The fraction of red galaxies in rich clusters has not changed since $z \sim 1$, suggesting that the environmental dependence of galaxy colors is already in place. Poor groups at $z \sim 1$ show a lower red fraction than rich clusters.

We found that the red sequence of galaxies in relatively poor systems appears to be truncated at $K_s = 21$, while that in richer systems exhibit a clear sequence down to fainter magnitudes. This confirms our earlier claim that the red sequence grows from bright magnitudes to faint magnitudes, and the build-up of the red sequence happens earlier in richer systems. Therefore, galaxies follow the environment-dependent down-sizing – massive galaxies in higher density environments are more evolved than less massive galaxies in less dense environments. Interestingly, the red sequence is truncated at brighter magnitudes than that found in the groups in the RDCSJ1252 field at $z = 1.24$. Although the groups have similar masses, the truncation magnitude is ∼1 mag brighter in the RDCSJ0910 field at $z = 1.1$.

Both the initial conditions of galaxy formation and the environmental effects determine the fate of a galaxy. It is difficult to disentangle these two effects, but $z > 1$ might be an era when the nature effects can be seen. Further detailed studies on $z > 1$ clusters would be a promising way of addressing this fundamental issue of galaxy evolution.

Acknowledgements. This study is based on data collected at Subaru Telescope, which is operated by the National Astronomical Observatory of Japan, and on observations made with the United Kingdom Infrared Telescope, which is operated by the Joint Astronomy Centre on behalf of the UK Particle Physics and Astronomy Research Council. The observations with the UKIRT 3.8m telescope were supported by NAOJ. We thank K. Motohara and M. Hayashi for providing the WFCAM *K*-band data and H. Furusawa and I. Tanaka for their help during the Suprime-Cam and MOIRCS observations, respectively. We thank the referee for his/her very helpful comments, which improved the paper. SAS's work was performed under the auspices of the US Department of Energy, National Nuclear Security Administration by the University of California, Lawrence Livermore National Laboratory under contract No. W-7405-Eng-48. This work was financially supported in part by a Grant-in-Aid for the Scientific Research (No. 15740126, 18684004) by the Japanese Ministry of Education, Culture, Sports and Science. AF acknowledges support from BMBF/DLR under grant 50 OR 0207, MPG and and a partial support from NASA grant NNX08AD93G, covering his stays at UMBC. Some of the data presented herein were obtained at the W.M. Keck Observatory, which is operated as a scientific partnership among the California Institute of Technology, the University of California and the National Aeronautics and Space Administration. The Observatory was made possible by the generous financial support of the W.M. Keck Foundation. Funding for the SDSS and SDSS-II has been provided by the Alfred P. Sloan Foundation, the Participating Institutions, the National Science Foundation, the US Department of Energy, the National Aeronautics and Space Administration, the Japanese Monbukagakusho, the Max Planck Society, and the Higher Education Funding Council for England. The SDSS Web Site is http://www.sdss.org/.

References

Adelman-McCarthy, J. K., Agüeros, M. A., Allam, S. S., et al. 2007, ApJS, 172, 634
Andreon, S., Puddu, E., de Propris, R., & Cuillandre, J.-C. 2008, MNRAS, 385, 979
Balogh, M. L., Smail, I., Bower, R. G., et al. 2002, ApJ, 566, 123
Beers, T. C., Flynn, K., & Gebhardt, K. 1990, AJ, 100, 32
Bertin, E., & Arnouts, S. 1996, A&AS, 117, 393
Blakeslee, J. P., Franx, M., Postman, M., et al. 2003, ApJ, 596, L143
Bruzual, G., & Charlot, S. 2003, MNRAS, 344, 1000
Cardelli, J. A., Clayton, G. C., & Mathis, J. S. 1989, ApJ, 345, 245
Carlberg, R. G., Yee, H. K. C., & Ellingson, E. 1997, ApJ, 478, 462
Chabrier, G. 2003, PASP, 115, 763
Charlot, S., & Fall, S. M. 2000, ApJ, 539, 718
Cooper, M. C., Newman, J. A., Coil, A. L., et al. 2007, MNRAS, 376, 1445
Cowie, L. L., & Barger, A. J. 2008, ArXiv e-prints, 806
Cucciati, O., Iovino, A., Marinoni, C., et al. 2006, A&A, 458, 39
De Lucia, G., Poggianti, B. M., Aragón-Salamanca, A., et al. 2007, MNRAS, 374, 809
Demarco, R., Rosati, P., Lidman, C., et al. 2007, ApJ, 663, 164
Diaferio, A., Kauffmann, G., Colberg, J. M., & White, S. D. M. 1999, MNRAS, 307, 537
Elbaz, D., Daddi, E., Le Borgne, D., et al. 2007, A&A, 468, 33
Finoguenov, A., Guzzo, L., Hasinger, G., et al. 2007, ApJS, 172, 182
Furusawa, H., Shimasaku, K., Doi, M., & Okamura, S. 2000, ApJ, 534, 624
Gerke, B. F., Newman, J. A., Faber, S. M., et al. 2007, MNRAS, 376, 1425
Gilbank, D. G., Yee, H. K. C., Ellingson, E., et al. 2008, ApJ, 673, 742
Holden, B. P., Stanford, S. A., Eisenhardt, P., & Dickinson, M. 2004, AJ, 127, 2484
Jarrett, T. H., Chester, T., Cutri, R., et al. 2000, AJ, 119, 2498
Kodama, T., Tanaka, M., Tamura, T., et al. 2005, PASJ, 57, 309
Koyama, Y., Kodama, T., Tanaka, M., Shimasaku, K., & Okamura, S. 2007, MNRAS, 382, 1719
Lidman, C., Rosati, P., Demarco, R., et al. 2004, A&A, 416, 829
Lidman, C., Rosati, P., Tanaka, M., et al. 2008, A&A, accepted
Madau, P. 1995, ApJ, 441, 18
Martínez, H. J., Zandivarez, A., Domínguez, M., Merchán, M. E., & Lambas, D. G. 2002, MNRAS, 333, L31
Mei, S. 2008, ApJ, submitted
Mei, S., Blakeslee, J. P., Stanford, S. A., et al. 2006a, ApJ, 639, 81
Mei, S., Holden, B. P., Blakeslee, J. P., et al. 2006b, ApJ, 644, 759
Merchán, M., & Zandivarez, A. 2002, MNRAS, 335, 216
Mullis, C. R., Rosati, P., Lamer, G., et al. 2005, ApJ, 623, L85
Nakata, F., Kodama, T., Shimasaku, K., et al. 2005, MNRAS, 357, 1357
Ramella, M., Pisani, A., & Geller, M. J. 1997, AJ, 113, 483
Rines, K., Geller, M. J., Kurtz, M. J., & Diaferio, A. 2005, AJ, 130, 1482
Rosati, P., della Ceca, R., Norman, C., & Giacconi, R. 1998, ApJ, 492, L21
Rosati, P., Tozzi, P., Ettori, S., et al. 2004, AJ, 127, 230
Schlegel, D. J., Finkbeiner, D. P., & Davis, M. 1998, ApJ, 500, 525
Stanford, S. A., Holden, B., Rosati, P., et al. 2002, AJ, 123, 619
Stanford, S. A., Eisenhardt, P. R., Brodwin, M., et al. 2005, ApJ, 634, L129
Stanford, S. A., Romer, A. K., Sabirli, K., et al. 2006, ApJ, 646, L13
Strauss, M. A., Weinberg, D. H., Lupton, R. H., et al. 2002, AJ, 124, 1810
Strazzullo, V., Rosati, P., Stanford, S. A., et al. 2006, A&A, 450, 909
Tanaka, M., Goto, T., Okamura, S., Shimasaku, K., & Brinkmann, J. 2004, AJ, 128, 2677
Tanaka, M., Kodama, T., Arimoto, N., et al. 2005, MNRAS, 362, 268
Tanaka, M., Kodama, T., Arimoto, N., et al. 2006, MNRAS, 365, 1392
Tanaka, M., Hoshi, T., Kodama, T., & Kashikawa, N. 2007a, MNRAS, 379, 1546
Tanaka, M., Kodama, T., Kajisawa, M., et al. 2007b, MNRAS, 377, 1206
Thomas, D., Maraston, C., Bender, R., & Mendes de Oliveira, C. 2005, ApJ, 621, 673
Tran, K.-V. H., Simard, L., Zabludoff, A. I., & Mulchaey, J. S. 2001, ApJ, 549, 172
Umetsu, K., Tanaka, M., Kodama, T., et al. 2005, PASJ, 57, 877
Yagi, M., Kashikawa, N., Sekiguchi, M., et al. 2002, AJ, 123, 66
York, D. G., Adelman, J., Anderson, Jr., J. E., et al. 2000, AJ, 120, 1579
Zabludoff, A. I., & Mulchaey, J. S. 1998, ApJ, 496, 39

Table 2. Spectroscopic catalog. The columns show object ID, coordinates in J2000, redshift, confidence flag (0 and 1 mean secure and possible redshifts, respectively), and aperture magnitudes within 2″ apertures and their errors. The systematic zero point errors are not included here. The redshift error does not include wavelength calibration error which is typically 0.3 Å.

ID	RA	Dec	redshift	flag	V	$\sigma(V)$	R	$\sigma(R)$	i	$\sigma(i)$	z	$\sigma(z)$	K	$\sigma(K)$
LRIS-8	09 10 47.5	54 17 04	$0.6122^{+0.0002}_{-0.0002}$	1	23.65	0.02	22.83	0.01	22.43	0.01	22.19	0.01	21.14	0.08
LRIS-9	09 10 51.7	54 22 18	$0.0000^{+0.0000}_{-0.0000}$	0	20.87	<0.01	20.02	<0.01	19.44	<0.01	19.11	<0.01	17.91	0.01
LRIS-11	09 10 38.2	54 22 39	$0.0000^{+0.0000}_{-0.0000}$	0	23.00	0.01	21.93	<0.01	20.27	<0.01	19.57	<0.01	18.55	0.01
LRIS-14	09 10 39.6	54 21 48	$0.0000^{+0.0000}_{-0.0000}$	0	21.74	<0.01	20.93	<0.01	20.08	<0.01	19.66	<0.01	19.03	0.02
LRIS-33	09 10 46.5	54 21 41	$1.1000^{+0.0001}_{-0.0001}$	0	24.66	0.04	23.70	0.01	22.94	0.01	22.04	0.01	20.68	0.06
LRIS-40	09 10 41.4	54 20 33	$0.6299^{+0.0002}_{-0.0002}$	0	23.27	0.01	22.45	0.01	22.02	0.01	21.78	0.01	20.84	0.06
LRIS-42	09 10 48.0	54 22 21	$0.0000^{+0.0000}_{-0.0000}$	0	22.73	0.01	22.53	0.01	22.33	0.01	21.83	0.01	20.44	0.05
LRIS-47	09 10 45.9	54 22 20	$1.1047^{+0.0006}_{-0.0024}$	0	26.04	0.13	24.18	0.02	23.65	0.02	22.50	0.02	20.69	0.06
LRIS-49	09 10 50.0	54 22 18	$0.2205^{+0.0001}_{-0.0002}$	0	22.23	<0.01	22.04	<0.01	21.94	<0.01	21.98	0.01	21.72	0.12
LRIS-60	09 10 41.1	54 22 19	$0.4352^{+0.0001}_{-0.0001}$	0	22.88	0.01	22.45	0.01	22.30	0.01	22.15	0.01	21.43	0.10
LRIS-72	09 10 44.3	54 22 07	$1.0950^{+0.0004}_{-0.0005}$	0	25.77	0.10	24.63	0.03	23.85	0.02	22.92	0.02	21.12	0.08
LRIS-73	09 10 38.9	54 21 17	$0.7597^{+0.0001}_{-0.0001}$	0	23.23	0.01	22.77	0.01	22.41	0.01	22.25	0.01	21.67	0.12
LRIS-106	09 10 09.3	54 17 14	$1.0935^{+0.0002}_{-0.0002}$	1	24.40	0.03	24.14	0.02	23.64	0.02	23.21	0.03	22.54	0.24
LRIS-115	09 10 40.5	54 20 50	$0.1174^{+0.0000}_{-0.0001}$	1	25.49	0.08	25.27	0.05	25.22	0.08	24.74	0.12	22.20	0.18
LRIS-149	09 10 48.1	54 17 24	$0.0000^{+0.0000}_{-0.0000}$	0	21.48	<0.01	21.51	<0.01	21.57	<0.01	21.71	0.01	22.60	0.25
LRIS-182	09 10 49.2	54 17 37	$0.2817^{+0.0001}_{-0.0000}$	0	22.77	0.01	22.49	0.01	22.37	0.01	22.28	0.01	21.65	0.12
LRIS-211	09 10 46.4	54 17 48	$0.0000^{+0.0000}_{-0.0000}$	0	22.96	0.01	22.13	<0.01	21.14	<0.01	20.62	<0.01	20.27	0.04
LRIS-314	09 10 31.9	54 18 18	$0.3480^{+0.0001}_{-0.0001}$	0	23.04	0.01	22.64	0.01	22.45	0.01	22.22	0.01	21.77	0.13
LRIS-338	09 10 50.8	54 18 29	$0.4213^{+0.0007}_{-0.0005}$	0	22.41	0.01	21.29	<0.01	20.82	<0.01	20.49	<0.01	19.22	0.02
LRIS-382	09 10 42.4	54 18 46	$0.0000^{+0.0000}_{-0.0000}$	0	20.21	<0.01	20.03	<0.01	20.06	<0.01	20.08	<0.01	20.60	0.05
LRIS-408	09 10 39.2	54 18 51	$0.5854^{+0.0003}_{-0.0001}$	0	23.16	0.01	22.53	0.01	22.27	0.01	22.16	0.01	21.80	0.13
LRIS-413	09 10 30.9	54 18 52	$0.0000^{+0.0000}_{-0.0000}$	0	23.68	0.02	22.79	0.01	21.52	<0.01	20.92	<0.01	20.47	0.05
LRIS-451	09 10 45.4	54 19 08	$0.7339^{+0.0001}_{-0.0001}$	0	23.02	0.01	22.39	0.01	21.84	<0.01	21.62	0.01	20.64	0.05
LRIS-488	09 10 33.1	54 19 15	$0.9268^{+0.0001}_{-0.0001}$	0	24.48	0.03	23.74	0.01	22.83	0.01	22.19	0.01	20.12	0.04
LRIS-496	09 10 34.7	54 19 22	$0.4665^{+0.0002}_{-0.0002}$	1	21.40	<0.01	20.75	<0.01	20.43	<0.01	20.26	<0.01	20.02	0.03
LRIS-497	09 10 31.5	54 19 18	$0.9243^{+0.0000}_{-0.0000}$	0	23.81	0.02	23.38	0.01	22.66	0.01	22.19	0.01	20.84	0.06
LRIS-527	09 10 39.7	54 19 27	$0.3326^{+0.0001}_{-0.0001}$	0	22.51	0.01	22.13	<0.01	21.97	<0.01	21.75	0.01	21.18	0.08
LRIS-595	09 10 38.9	54 19 42	$0.4208^{+0.0001}_{-0.0001}$	0	22.82	0.01	22.34	0.01	22.12	0.01	21.85	0.01	21.00	0.07
LRIS-598	09 10 33.2	54 19 50	$0.4346^{+0.0001}_{-0.0001}$	0	21.82	<0.01	21.18	<0.01	20.90	<0.01	20.65	<0.01	19.55	0.03
LRIS-604	09 10 41.5	54 19 48	$0.7849^{+0.0008}_{-0.0001}$	0	21.69	<0.01	21.57	<0.01	21.23	<0.01	20.86	<0.01	19.65	0.03
LRIS-623	09 10 38.3	54 19 51	$0.7614^{+0.0001}_{-0.0003}$	0	23.21	0.01	22.65	0.01	22.14	0.01	21.94	0.01	20.79	0.06
LRIS-626	09 10 30.8	54 19 56	$0.3480^{+0.0002}_{-0.0007}$	0	22.30	0.01	21.56	<0.01	21.08	<0.01	20.65	<0.01	18.97	0.02
LRIS-664	09 10 49.6	54 20 05	$0.5239^{+0.0001}_{-0.0001}$	0	23.14	0.01	22.43	0.01	22.16	0.01	21.93	0.01	20.94	0.07
LRIS-678	09 10 40.1	54 20 10	$1.0916^{+0.0006}_{-0.0003}$	1	23.78	0.02	23.34	0.01	22.85	0.01	22.27	0.01	20.89	0.07
LRIS-686	09 10 55.5	54 20 11	$0.7856^{+0.0000}_{-0.0000}$	0	23.66	0.02	23.19	0.01	22.72	0.01	22.53	0.02	21.92	0.15
LRIS-687	09 10 38.9	54 20 15	$0.7360^{+0.0000}_{-0.0000}$	0	23.61	0.02	22.88	0.01	22.26	0.01	21.96	0.01	20.57	0.05
LRIS-707	09 10 22.8	54 20 21	$0.1229^{+0.0001}_{-0.0001}$	0	20.87	<0.01	20.63	<0.01	20.45	<0.01	20.34	<0.01	19.91	0.03
LRIS-709	09 10 51.8	54 20 21	$0.0000^{+0.0000}_{-0.0000}$	0	21.86	<0.01	21.04	<0.01	20.10	<0.01	19.70	<0.01	19.12	0.02
LRIS-714	09 11 03.8	54 20 26	$0.4362^{+0.0001}_{-0.0001}$	0	21.91	<0.01	21.34	<0.01	21.15	<0.01	20.92	<0.01	20.12	0.04
LRIS-732	09 10 27.9	54 20 34	$0.3749^{+0.0001}_{-0.0003}$	0	21.52	<0.01	20.90	<0.01	20.55	<0.01	20.24	<0.01	18.94	0.02
LRIS-760	09 10 30.0	54 20 33	$0.9286^{+0.0001}_{-0.0001}$	0	23.41	0.01	22.86	0.01	22.08	0.01	21.56	0.01	19.93	0.03
LRIS-764	09 10 41.9	54 20 32	$0.7643^{+0.0005}_{-0.0005}$	0	23.46	0.01	22.84	0.01	22.21	0.01	21.97	0.01	20.91	0.07
LRIS-769	09 10 33.2	54 20 35	$0.0000^{+0.0000}_{-0.0000}$	0	21.36	<0.01	21.12	<0.01	21.00	<0.01	20.96	<0.01	21.13	0.08
LRIS-779	09 10 52.8	54 20 33	$0.5610^{+0.0002}_{-0.0001}$	0	23.27	0.01	22.59	0.01	22.34	0.01	22.23	0.01	21.59	0.11
LRIS-785	09 10 39.5	54 20 40	$0.7829^{+0.0000}_{-0.0000}$	0	23.41	0.01	22.95	0.01	22.43	0.01	22.22	0.01	21.35	0.09
LRIS-793	09 10 39.8	54 20 35	$0.9120^{+0.0001}_{-0.0001}$	0	22.18	<0.01	22.12	<0.01	22.19	0.01	21.76	0.01	20.74	0.06
LRIS-795	09 10 42.8	54 20 37	$1.1054^{+0.0002}_{-0.0002}$	0	23.38	0.01	22.97	0.01	22.48	0.01	21.82	0.01	20.32	0.04
LRIS-805	09 10 55.9	54 20 49	$0.6287^{+0.0001}_{-0.0001}$	0	22.39	0.01	21.49	<0.01	20.94	<0.01	20.62	<0.01	19.39	0.02
LRIS-814	09 10 26.1	54 20 44	$1.0309^{+0.0000}_{-0.0001}$	0	24.20	0.03	23.66	0.01	23.02	0.01	22.46	0.02	20.68	0.06
LRIS-817	09 10 57.9	54 20 41	$0.4292^{+0.0000}_{-0.0000}$	0	23.23	0.01	22.74	0.01	22.61	0.01	22.44	0.02	21.95	0.15
LRIS-819	09 10 57.7	54 20 46	$0.7823^{+0.0001}_{-0.0001}$	1	23.52	0.01	23.00	0.01	22.44	0.01	22.19	0.01	21.28	0.09
LRIS-824	09 10 36.3	54 20 53	$0.9276^{+0.0000}_{-0.0000}$	1	24.32	0.03	23.54	0.01	22.85	0.01	22.46	0.02	20.75	0.06
LRIS-830	09 10 23.4	54 20 48	$0.4282^{+0.0001}_{-0.0001}$	0	23.02	0.01	22.46	0.01	22.23	0.01	21.99	0.01	21.15	0.08

Table 2. continued.

ID	RA	Dec	redshift	flag	V	$\sigma(V)$	R	$\sigma(R)$	i	$\sigma(i)$	z	$\sigma(z)$	K	$\sigma(K)$
LRIS-840	09 10 39.2	54 20 56	$0.6272^{+0.0002}_{-0.0002}$	0	23.51	0.01	22.41	0.01	21.73	<0.01	21.27	0.01	19.42	0.02
LRIS-841	09 10 53.0	54 21 16	$0.8111^{+0.0006}_{-0.0004}$	0	23.37	0.01	22.90	0.01	22.36	0.01	22.09	0.01	20.93	0.07
LRIS-842	09 11 01.9	54 20 51	$0.8030^{+0.0000}_{-0.0001}$	0	23.09	0.01	22.70	0.01	22.27	0.01	22.06	0.01	21.36	0.09
LRIS-844	09 10 22.4	54 20 55	$0.4335^{+0.0001}_{-0.0001}$	0	22.75	0.01	22.31	0.01	22.15	0.01	22.01	0.01	21.45	0.10
LRIS-846	09 10 38.1	54 21 05	$0.6297^{+0.0001}_{-0.0001}$	0	24.01	0.02	22.85	0.01	22.09	0.01	21.53	0.01	19.42	0.02
LRIS-847	09 10 38.8	54 20 55	$0.5636^{+0.0004}_{-0.0004}$	0	23.60	0.01	23.03	0.01	22.77	0.01	22.69	0.02	21.82	0.14
LRIS-855	09 10 55.5	54 20 58	$0.2298^{+0.0029}_{-0.0001}$	0	22.33	0.01	22.13	<0.01	22.07	0.01	22.09	0.01	22.00	0.16
LRIS-858	09 11 06.7	54 20 56	$0.9577^{+0.0000}_{-0.0000}$	0	23.29	0.01	22.99	0.01	22.38	0.01	22.07	0.01	21.30	0.09
LRIS-862	09 10 46.2	54 21 05	$0.0000^{+0.0000}_{-0.0000}$	0	22.03	<0.01	21.18	<0.01	20.12	<0.01	19.67	<0.01	18.91	0.02
LRIS-866	09 10 38.9	54 21 01	$0.7587^{+0.0001}_{-0.0003}$	0	24.14	0.02	23.31	0.01	22.58	0.01	22.24	0.01	20.52	0.05
LRIS-871	09 10 29.4	54 21 08	$0.4218^{+0.0002}_{-0.0005}$	0	22.69	0.01	21.77	<0.01	21.39	<0.01	21.13	0.01	20.02	0.03
LRIS-872	09 10 58.8	54 21 02	$0.8044^{+0.0001}_{-0.0003}$	0	23.01	0.01	22.48	0.01	21.88	<0.01	21.62	0.01	20.41	0.05
LRIS-878	09 10 22.6	54 21 07	$0.0000^{+0.0000}_{-0.0000}$	0	23.07	0.01	22.21	<0.01	21.09	<0.01	20.55	<0.01	20.10	0.04
LRIS-889	09 10 51.3	54 21 12	$0.0000^{+0.0000}_{-0.0000}$	0	20.47	<0.01	20.21	<0.01	20.17	<0.01	20.10	<0.01	20.37	0.04
LRIS-894	09 10 38.2	54 21 08	$1.1014^{+0.0000}_{-0.0000}$	0	23.94	0.02	23.51	0.01	23.02	0.01	22.52	0.02	21.41	0.10
LRIS-923	09 10 38.2	54 21 10	$0.8601^{+0.0008}_{-0.0022}$	1	24.54	0.03	24.09	0.02	23.45	0.02	23.15	0.03	22.24	0.19
LRIS-932	09 10 51.2	54 21 19	$0.8104^{+0.0001}_{-0.0012}$	0	24.54	0.03	23.58	0.01	22.63	0.01	22.10	0.01	20.64	0.05
LRIS-937	09 10 46.5	54 21 22	$0.0000^{+0.0000}_{-0.0000}$	0	24.14	0.02	23.15	0.01	21.73	<0.01	21.00	0.01	20.36	0.04
LRIS-938	09 10 51.6	54 21 23	$0.6454^{+0.0004}_{-0.0002}$	0	22.30	0.01	21.68	<0.01	21.38	<0.01	21.20	0.01	19.99	0.03
LRIS-944	09 10 24.2	54 21 38	$0.4340^{+0.0003}_{-0.0002}$	0	22.07	<0.01	20.98	<0.01	20.50	<0.01	20.15	<0.01	18.81	0.02
LRIS-954	09 10 46.1	54 21 31	$0.1421^{+0.0001}_{-0.0000}$	0	21.34	<0.01	21.20	<0.01	20.96	<0.01	20.92	<0.01	20.46	0.05
LRIS-955	09 10 42.0	54 21 30	$0.5976^{+0.0002}_{-0.0006}$	0	22.48	0.01	22.05	<0.01	21.64	<0.01	21.44	0.01	20.16	0.04
LRIS-980	09 11 06.7	54 21 41	$0.0000^{+0.0000}_{-0.0000}$	0	21.46	<0.01	20.66	<0.01	19.97	<0.01	19.48	<0.01	18.99	0.02
LRIS-983	09 10 51.0	54 21 39	$1.3842^{+0.0001}_{-0.0001}$	0	23.29	0.01	22.92	0.01	22.66	0.01	22.17	0.01	21.21	0.08
LRIS-989	09 10 51.1	54 21 46	$0.7598^{+0.0001}_{-0.0001}$	0	22.52	0.01	21.95	<0.01	21.37	<0.01	21.12	0.01	19.82	0.03
LRIS-1000	09 10 37.9	54 22 10	$0.0000^{+0.0000}_{-0.0000}$	0	22.45	0.01	21.58	<0.01	20.40	<0.01	19.88	<0.01	19.25	0.02
LRIS-1003	09 10 18.3	54 21 42	$0.6277^{+0.0001}_{-0.0001}$	0	23.83	0.02	22.82	0.01	22.17	0.01	21.81	0.01	20.26	0.04
LRIS-1006	09 10 24.2	54 21 46	$0.4336^{+0.0001}_{-0.0002}$	0	22.06	<0.01	21.55	<0.01	21.38	<0.01	21.20	0.01	20.53	0.05
LRIS-1007	09 10 50.2	54 21 45	$0.0000^{+0.0000}_{-0.0000}$	0	21.29	<0.01	20.87	<0.01	20.69	<0.01	20.57	<0.01	20.60	0.05
LRIS-1013	09 10 42.7	54 21 44	$1.0939^{+0.0013}_{-0.0011}$	0	25.90	0.11	24.72	0.03	23.88	0.02	22.89	0.02	20.72	0.06
LRIS-1020	09 10 59.9	54 21 46	$0.8111^{+0.0003}_{-0.0002}$	0	24.26	0.03	23.51	0.01	22.66	0.01	22.09	0.01	20.42	0.05
LRIS-1031	09 10 46.5	54 21 48	$0.7607^{+0.0000}_{-0.0000}$	0	23.75	0.02	23.17	0.01	22.66	0.01	22.34	0.01	21.13	0.08
LRIS-1035	09 10 35.4	54 21 57	$0.4207^{+0.0001}_{-0.0001}$	0	22.50	0.01	21.93	<0.01	21.70	<0.01	21.46	0.01	20.47	0.05
LRIS-1038	09 11 02.6	54 21 53	$0.9610^{+0.0001}_{-0.0001}$	1	24.58	0.04	24.28	0.02	23.71	0.02	23.38	0.04	22.66	0.26
LRIS-1049	09 10 25.4	54 22 00	$0.4317^{+0.0001}_{-0.0001}$	0	22.09	<0.01	21.49	<0.01	21.24	<0.01	20.98	<0.01	19.93	0.03
LRIS-1052	09 10 34.1	54 21 59	$0.4328^{+0.0001}_{-0.0000}$	0	22.85	0.01	22.32	0.01	22.10	0.01	21.88	0.01	21.07	0.07
LRIS-1064	09 10 37.5	54 22 18	$0.4354^{+0.0002}_{-0.0002}$	0	22.68	0.01	21.87	<0.01	21.46	<0.01	21.08	0.01	19.47	0.02
LRIS-1075	09 10 44.8	54 22 00	$1.1109^{+0.0013}_{-0.0021}$	0	26.00	0.12	24.43	0.03	23.54	0.02	22.51	0.02	20.73	0.06
LRIS-1079	09 10 41.6	54 22 02	$1.1157^{+0.0001}_{-0.0001}$	1	24.30	0.03	23.96	0.02	23.52	0.02	23.04	0.03	21.80	0.13
LRIS-1091	09 11 07.8	54 22 09	$0.0000^{+0.0000}_{-0.0000}$	0	23.19	0.01	22.30	<0.01	21.19	<0.01	20.62	<0.01	20.19	0.04
LRIS-1101	09 10 45.9	54 22 07	$1.0988^{+0.0003}_{-0.0003}$	0	25.60	0.09	24.14	0.02	23.28	0.01	22.24	0.01	20.31	0.04
LRIS-1102	09 11 00.2	54 22 17	$0.2919^{+0.0001}_{-0.0002}$	0	22.24	<0.01	21.82	<0.01	21.53	<0.01	21.26	0.01	20.20	0.04
LRIS-1104	09 11 00.8	54 22 12	$0.4215^{+0.0002}_{-0.0006}$	0	23.41	0.01	22.65	0.01	22.28	0.01	21.93	0.01	20.71	0.06
LRIS-1105	09 10 55.9	54 22 14	$0.4340^{+0.0002}_{-0.0001}$	0	22.64	0.01	22.12	<0.01	21.90	<0.01	21.64	0.01	20.74	0.06
LRIS-1107	09 10 40.8	54 22 09	$1.1014^{+0.0001}_{-0.0001}$	0	23.68	0.02	23.28	0.01	22.82	0.01	22.20	0.01	20.64	0.05
LRIS-1110	09 11 00.1	54 22 11	$0.9628^{+0.0000}_{-0.0000}$	0	23.21	0.01	23.05	0.01	22.62	0.01	22.41	0.02	21.86	0.14
LRIS-1121	09 10 47.6	54 22 14	$1.3409^{+0.0001}_{-0.0001}$	0	24.12	0.02	23.42	0.01	22.90	0.01	22.11	0.01	19.93	0.03
LRIS-1122	09 10 58.5	54 22 16	$0.4148^{+0.0002}_{-0.0002}$	0	22.71	0.01	22.19	<0.01	21.98	<0.01	21.76	0.01	20.93	0.07
LRIS-1129	09 11 05.0	54 22 17	$0.3992^{+0.0001}_{-0.0001}$	0	22.76	0.01	22.35	0.01	22.19	0.01	21.98	0.01	21.39	0.10
LRIS-1138	09 10 26.7	54 22 24	$0.2875^{+0.0001}_{-0.0002}$	0	21.66	<0.01	21.24	<0.01	20.99	<0.01	20.76	<0.01	19.75	0.03
LRIS-1142	09 10 43.0	54 22 35	$0.4297^{+0.0004}_{-0.0004}$	0	22.06	<0.01	21.51	<0.01	21.31	<0.01	21.09	0.01	20.24	0.04
LRIS-1259	09 11 05.0	54 25 40	$1.0171^{+0.0001}_{-0.0000}$	0	23.97	0.02	23.84	0.02	23.36	0.02	23.07	0.03	23.14	0.38
LRIS-1315	09 10 57.1	54 25 17	$0.5221^{+0.0001}_{-0.0001}$	0	22.58	0.01	21.80	<0.01	21.51	<0.01	21.26	0.01	20.26	0.04
LRIS-1370	09 11 00.9	54 25 13	$0.9812^{+0.0001}_{-0.0001}$	0	24.17	0.02	23.55	0.01	22.76	0.01	22.11	0.01	20.23	0.04
LRIS-1391	09 10 54.8	54 25 17	$0.4936^{+0.0002}_{-0.0003}$	0	23.49	0.01	23.00	0.01	22.81	0.01	22.68	0.02	21.70	0.12

Table 2. continued.

ID	RA	Dec	redshift	flag	V	$\sigma(V)$	R	$\sigma(R)$	i	$\sigma(i)$	z	$\sigma(z)$	K	$\sigma(K)$
LRIS-1410	09 11 05.2	54 25 09	$0.5984^{+0.0001}_{-0.0001}$	0	23.57	0.01	23.04	0.01	22.78	0.01	22.77	0.02	22.01	0.16
LRIS-1412	09 10 55.6	54 24 55	$0.3348^{+0.0001}_{-0.0001}$	0	22.50	0.01	22.15	<0.01	22.01	0.01	21.75	0.01	21.29	0.09
LRIS-1452	09 10 56.3	54 24 41	$0.2653^{+0.0000}_{-0.0000}$	0	21.86	<0.01	21.28	<0.01	20.93	<0.01	20.66	<0.01	19.69	0.03
LRIS-1454	09 10 25.2	54 23 13	$0.7859^{+0.0007}_{-0.0008}$	0	24.43	0.03	23.73	0.01	22.86	0.01	22.32	0.01	20.59	0.05
LRIS-1463	09 10 52.8	54 24 42	$0.9082^{+0.0001}_{-0.0001}$	1	24.47	0.03	24.01	0.02	23.53	0.02	23.26	0.03	22.31	0.20
LRIS-1515	09 10 55.4	54 23 13	$0.0000^{+0.0000}_{-0.0000}$	0	22.24	<0.01	21.20	<0.01	20.08	<0.01	19.65	<0.01	18.71	0.02
LRIS-1541	09 10 30.9	54 24 33	$0.7837^{+0.0001}_{-0.0002}$	0	23.83	0.02	23.16	0.01	22.38	0.01	22.00	0.01	20.46	0.05
LRIS-1562	09 10 42.6	54 24 04	$0.1422^{+0.0002}_{-0.0004}$	0	21.10	<0.01	20.88	<0.01	20.68	<0.01	20.59	<0.01	20.08	0.04
LRIS-1601	09 10 34.5	54 24 10	$0.3397^{+0.0000}_{-0.0001}$	0	22.20	<0.01	21.89	<0.01	21.79	<0.01	21.57	0.01	20.95	0.07
LRIS-1616	09 10 57.7	54 23 32	$0.5097^{+0.0003}_{-0.0002}$	0	23.37	0.01	22.83	0.01	22.68	0.01	22.63	0.02	22.63	0.26
LRIS-1632	09 10 33.5	54 23 31	$0.4067^{+0.0001}_{-0.0001}$	0	23.41	0.01	22.78	0.01	22.45	0.01	22.12	0.01	20.71	0.06
LRIS-1652	09 11 00.5	54 23 60	$0.2204^{+0.0001}_{-0.0001}$	0	22.10	<0.01	21.85	<0.01	21.65	<0.01	21.56	0.01	21.03	0.07
LRIS-1654	09 11 04.3	54 24 02	$0.5631^{+0.0004}_{-0.0006}$	0	23.49	0.01	22.33	0.01	21.64	<0.01	21.20	0.01	19.81	0.03
LRIS-1707	09 10 35.2	54 23 47	$0.9284^{+0.0003}_{-0.0003}$	0	24.07	0.02	23.14	0.01	22.23	0.01	21.41	0.01	19.55	0.03
LRIS-1708	09 10 37.8	54 23 44	$0.0000^{+0.0000}_{-0.0000}$	0	22.18	<0.01	21.27	<0.01	20.16	<0.01	19.73	<0.01	18.76	0.02
LRIS-1710	09 10 59.7	54 23 38	$0.3326^{+0.0000}_{-0.0000}$	0	21.53	<0.01	20.66	<0.01	20.27	<0.01	19.92	<0.01	18.66	0.01
LRIS-1726	09 10 20.4	54 23 37	$0.5625^{+0.0004}_{-0.0003}$	0	23.61	0.02	22.83	0.01	22.51	0.01	22.25	0.01	21.08	0.08
LRIS-1745	09 10 43.7	54 23 35	$0.0000^{+0.0000}_{-0.0000}$	0	21.09	<0.01	20.35	<0.01	19.90	<0.01	19.68	<0.01	19.11	0.02
LRIS-1769	09 11 00.9	54 23 24	$0.0000^{+0.0000}_{-0.0000}$	0	24.28	0.03	23.36	0.01	22.27	0.01	21.69	0.01	21.39	0.10
LRIS-1778	09 10 55.0	54 23 14	$0.6557^{+0.0002}_{-0.0002}$	0	23.95	0.02	22.88	0.01	22.16	0.01	21.70	0.01	19.89	0.03
LRIS-1821	09 10 26.4	54 23 13	$0.7860^{+0.0002}_{-0.0004}$	0	24.82	0.04	23.97	0.02	23.08	0.01	22.62	0.02	20.92	0.07
LRIS-1822	09 10 34.2	54 23 04	$0.0000^{+0.0000}_{-0.0000}$	1	22.20	<0.01	21.56	<0.01	21.17	<0.01	20.91	<0.01	20.69	0.06
LRIS-1828	09 10 54.8	54 23 06	$0.4358^{+0.0006}_{-0.0003}$	0	22.34	0.01	22.02	<0.01	21.89	<0.01	21.80	0.01	21.31	0.09
LRIS-1861	09 11 06.2	54 23 02	$1.2743^{+0.0008}_{-0.0012}$	0	24.64	0.04	23.60	0.01	22.80	0.01	21.74	0.01	19.94	0.03
LRIS-1865	09 10 59.9	54 22 52	$0.8115^{+0.0003}_{-0.0002}$	0	23.38	0.01	22.90	0.01	22.27	0.01	21.99	0.01	20.63	0.05
LRIS-1867	09 11 00.4	54 22 52	$0.6813^{+0.0001}_{-0.0001}$	0	24.06	0.02	23.28	0.01	22.74	0.01	22.45	0.02	21.15	0.08
LRIS-1872	09 10 18.3	54 23 02	$0.3211^{+0.0000}_{-0.0001}$	0	22.00	<0.01	21.41	<0.01	21.04	<0.01	20.63	<0.01	19.15	0.02
LRIS-1894	09 11 02.1	54 22 52	$0.1427^{+0.0001}_{-0.0002}$	0	22.24	<0.01	22.17	<0.01	21.99	<0.01	21.97	0.01	21.86	0.14
LRIS-1898	09 11 01.2	54 22 49	$0.9324^{+0.0003}_{-0.0012}$	0	23.35	0.01	22.94	0.01	22.26	0.01	21.78	0.01	20.42	0.05
LRIS-1902	09 10 48.5	54 22 49	$0.8855^{+0.0000}_{-0.0000}$	0	24.13	0.02	23.60	0.01	22.85	0.01	22.39	0.01	20.76	0.06
LRIS-1905	09 11 03.7	54 22 48	$0.0000^{+0.0000}_{-0.0000}$	0	21.79	<0.01	21.04	<0.01	20.42	<0.01	20.12	<0.01	19.68	0.03
LRIS-1907	09 10 46.3	54 22 45	$0.5180^{+0.0001}_{-0.0001}$	0	23.56	0.01	22.57	0.01	22.13	0.01	21.74	0.01	20.17	0.04
LRIS-1911	09 10 40.0	54 22 46	$0.7376^{+0.0001}_{-0.0001}$	1	24.86	0.05	23.96	0.02	23.21	0.01	22.83	0.02	20.95	0.07
LRIS-1921	09 10 38.2	54 22 39	$0.0000^{+0.0000}_{-0.0000}$	0	23.00	0.01	21.93	<0.01	20.27	<0.01	19.57	<0.01	18.55	0.01
LRIS-1937	09 10 36.7	54 22 37	$0.9031^{+0.0004}_{-0.0006}$	0	24.71	0.04	24.09	0.02	23.34	0.02	22.79	0.02	21.56	0.11
LRIS-1938	09 10 39.2	54 22 28	$0.1424^{+0.0003}_{-0.0001}$	0	23.10	0.01	22.85	0.01	22.68	0.01	22.57	0.02	22.28	0.20
LRIS-1939	09 10 56.2	54 22 36	$0.7719^{+0.0001}_{-0.0002}$	0	23.20	0.01	22.41	0.01	21.60	<0.01	21.19	0.01	19.75	0.03
LRIS-1940	09 10 21.4	54 22 37	$0.2997^{+0.0001}_{-0.0001}$	0	23.00	0.01	22.60	0.01	22.17	0.01	21.83	0.01	20.43	0.05
LRIS-1955	09 11 06.9	54 22 25	$0.8755^{+0.0003}_{-0.0001}$	1	24.85	0.05	24.02	0.02	22.80	0.01	22.13	0.01	21.74	0.13
LRIS-1971	09 10 48.2	54 22 25	$1.0975^{+0.0005}_{-0.0014}$	0	24.75	0.04	24.17	0.02	23.56	0.02	22.82	0.02	21.18	0.08
LRIS-5023	09 10 48.2	54 22 30	$1.0975^{+0.0002}_{-0.0001}$	0	25.69	0.09	24.58	0.03	23.69	0.02	22.71	0.02	20.40	0.05
LRIS-5077	09 10 51.4	54 21 46	$0.7594^{+0.0001}_{-0.0001}$	0	24.54	0.03	24.02	0.02	23.50	0.02	22.96	0.02	21.18	0.08
LRIS-5089	09 10 45.9	54 21 37	$0.1419^{+0.0001}_{-0.0001}$	0	26.22	0.15	25.58	0.07	24.86	0.06	23.86	0.05	21.49	0.10
LRIS-5092	09 10 42.2	54 21 29	$0.5979^{+0.0001}_{-0.0002}$	0	23.90	0.02	23.56	0.01	22.94	0.01	22.60	0.02	21.59	0.11
LRIS-5096	09 10 47.4	54 21 45	$0.7600^{+0.0002}_{-0.0005}$	1	25.92	0.12	25.23	0.05	24.52	0.04	23.73	0.05	21.99	0.16
LRIS-5161	09 10 30.0	54 18 48	$1.1130^{+0.0001}_{-0.0001}$	0	23.94	0.02	23.62	0.01	23.21	0.01	22.70	0.02	21.61	0.11
FOCAS-1-1	09 10 44.5	54 21 49	$0.4360^{+0.0002}_{-0.0001}$	0	21.59	<0.01	20.75	<0.01	20.33	<0.01	19.94	<0.01	18.32	0.01
FOCAS-1-3	09 10 40.9	54 24 35	$1.2099^{+0.0002}_{-0.0002}$	1	26.49	0.19	25.53	0.07	24.73	0.05	23.81	0.05	21.63	0.12
FOCAS-1-4	09 10 42.1	54 24 01	$1.1056^{+0.0018}_{-0.0007}$	1	25.97	0.12	24.76	0.03	24.05	0.03	23.09	0.03	21.42	0.10
FOCAS-1-5	09 10 41.2	54 23 41	$1.1051^{+0.0007}_{-0.0003}$	0	24.73	0.04	24.56	0.03	24.17	0.03	23.63	0.04	22.68	0.27
FOCAS-1-6	09 10 45.7	54 23 29	$1.1051^{+0.0002}_{-0.0002}$	0	25.39	0.07	23.90	0.02	22.94	0.01	21.83	0.01	19.69	0.03
FOCAS-1-7	09 10 40.7	54 23 01	$1.1015^{+0.0005}_{-0.0005}$	0	27.06	0.30	25.61	0.07	24.63	0.05	23.60	0.04	21.42	0.10
FOCAS-1-8a	09 10 44.4	54 22 11	$1.1135^{+0.0009}_{-0.0025}$	1	25.66	0.09	24.86	0.04	24.29	0.03	23.50	0.04	21.61	0.11
FOCAS-1-8b	09 10 44.2	54 22 18	$0.0000^{+0.0000}_{-0.0000}$	1	18.80	<0.01	18.41	<0.01	18.68	<0.01	18.34	<0.01	16.81	0.01
FOCAS-1-9	09 10 47.4	54 21 31	$0.4347^{+0.0001}_{-0.0000}$	0	23.32	0.01	22.81	0.01	22.63	0.01	22.43	0.02	21.81	0.13

Table 2. continued.

ID	RA	Dec	redshift	flag	V	$\sigma(V)$	R	$\sigma(R)$	i	$\sigma(i)$	z	$\sigma(z)$	K	$\sigma(K)$
FOCAS-1-10	09 10 29.7	54 21 12	$1.1212^{+0.0003}_{-0.0003}$	1	25.85	0.11	24.70	0.03	23.84	0.02	22.98	0.02	20.85	0.06
FOCAS-1-12	09 10 34.2	54 20 31	$1.0975^{+0.0003}_{-0.0002}$	0	26.42	0.18	24.84	0.04	23.96	0.03	22.85	0.02	20.95	0.07
FOCAS-1-13	09 10 42.7	54 20 11	$1.0969^{+0.0002}_{-0.0003}$	0	26.41	0.18	25.09	0.05	24.14	0.03	23.00	0.03	20.77	0.06
FOCAS-1-14	09 10 39.0	54 19 56	$1.1002^{+0.0008}_{-0.0005}$	0	25.70	0.10	24.17	0.02	23.25	0.01	22.19	0.01	20.06	0.04
FOCAS-1-15	09 10 38.7	54 19 34	$0.9075^{+0.0010}_{-0.0005}$	0	25.53	0.08	24.44	0.03	23.50	0.02	22.74	0.02	21.03	0.07
FOCAS-1-16	09 10 41.8	54 19 13	$0.7835^{+0.0001}_{-0.0004}$	0	24.20	0.03	23.73	0.01	23.33	0.01	23.11	0.03	22.74	0.28
FOCAS-2-1	09 10 44.5	54 21 49	$0.4355^{+0.0003}_{-0.0001}$	0	21.59	<0.01	20.75	<0.01	20.33	<0.01	19.94	<0.01	18.32	0.01
FOCAS-2-3	09 10 45.6	54 24 49	$1.1259^{+0.0001}_{-0.0001}$	1	25.31	0.07	24.63	0.03	23.87	0.02	23.04	0.03	21.22	0.08
FOCAS-2-4	09 10 39.1	54 24 29	$0.4082^{+0.0001}_{-0.0000}$	0	22.30	0.01	21.66	<0.01	21.35	<0.01	21.05	0.01	19.92	0.03
FOCAS-2-5	09 10 41.8	54 24 04	$1.3499^{+0.0000}_{-0.0000}$	0	24.87	0.05	24.54	0.03	24.18	0.03	23.45	0.04	22.34	0.21
FOCAS-2-6	09 10 29.0	54 23 45	$0.7837^{+0.0001}_{-0.0001}$	0	25.08	0.06	24.25	0.02	23.30	0.01	22.88	0.02	21.72	0.13
FOCAS-2-7	09 10 46.4	54 23 37	$1.0905^{+0.0001}_{-0.0001}$	0	24.40	0.03	23.53	0.01	22.77	0.01	21.86	0.01	20.24	0.04
FOCAS-2-8	09 10 46.3	54 23 20	$0.2305^{+0.0000}_{-0.0000}$	0	23.09	0.01	22.82	0.01	22.74	0.01	22.76	0.02	22.48	0.23
FOCAS-2-9	09 10 45.7	54 22 57	$1.1038^{+0.0006}_{-0.0010}$	1	26.90	0.27	25.51	0.07	24.67	0.05	23.63	0.04	21.72	0.12
FOCAS-2-11	09 10 45.9	54 22 07	$1.0991^{+0.0022}_{-0.0018}$	0	25.60	0.09	24.14	0.02	23.28	0.01	22.24	0.01	20.31	0.04
FOCAS-2-12	09 10 49.2	54 21 05	$0.7848^{+0.0000}_{-0.0005}$	0	24.65	0.04	24.15	0.02	23.69	0.02	23.49	0.04	23.04	0.36
FOCAS-2-13b	09 10 52.5	54 20 47	$0.0000^{+0.0000}_{-0.0000}$	0	20.82	<0.01	20.31	<0.01	20.06	<0.01	19.88	<0.01	19.88	0.03
FOCAS-2-16	09 10 32.2	54 19 48	$0.9274^{+0.0001}_{-0.0001}$	0	25.26	0.06	23.95	0.02	22.91	0.01	22.04	0.01	20.17	0.04
FOCAS-2-17	09 10 37.9	54 19 31	$0.7357^{+0.0001}_{-0.0001}$	0	24.33	0.03	23.81	0.02	23.48	0.02	23.37	0.04	22.66	0.26
FOCAS-2-18	09 10 40.3	54 19 10	$0.6309^{+0.0002}_{-0.0001}$	0	25.45	0.08	24.68	0.03	24.43	0.04	24.36	0.08	23.50	0.50